

NASA Technical Memorandum 102627

**DETERMINATION OF SHUTTLE ORBITER
CENTER OF GRAVITY FROM FLIGHT
MEASUREMENTS**

E. W. Hinson

J. Y. Nicholson

R. C. Blanchard

**(NASA-TM-102627) DETERMINATION OF SHUTTLE
ORBITER CENTER OF GRAVITY FROM FLIGHT
MEASUREMENTS (NASA) 55 p**

CSCL 22B

N91-16058

Unclass

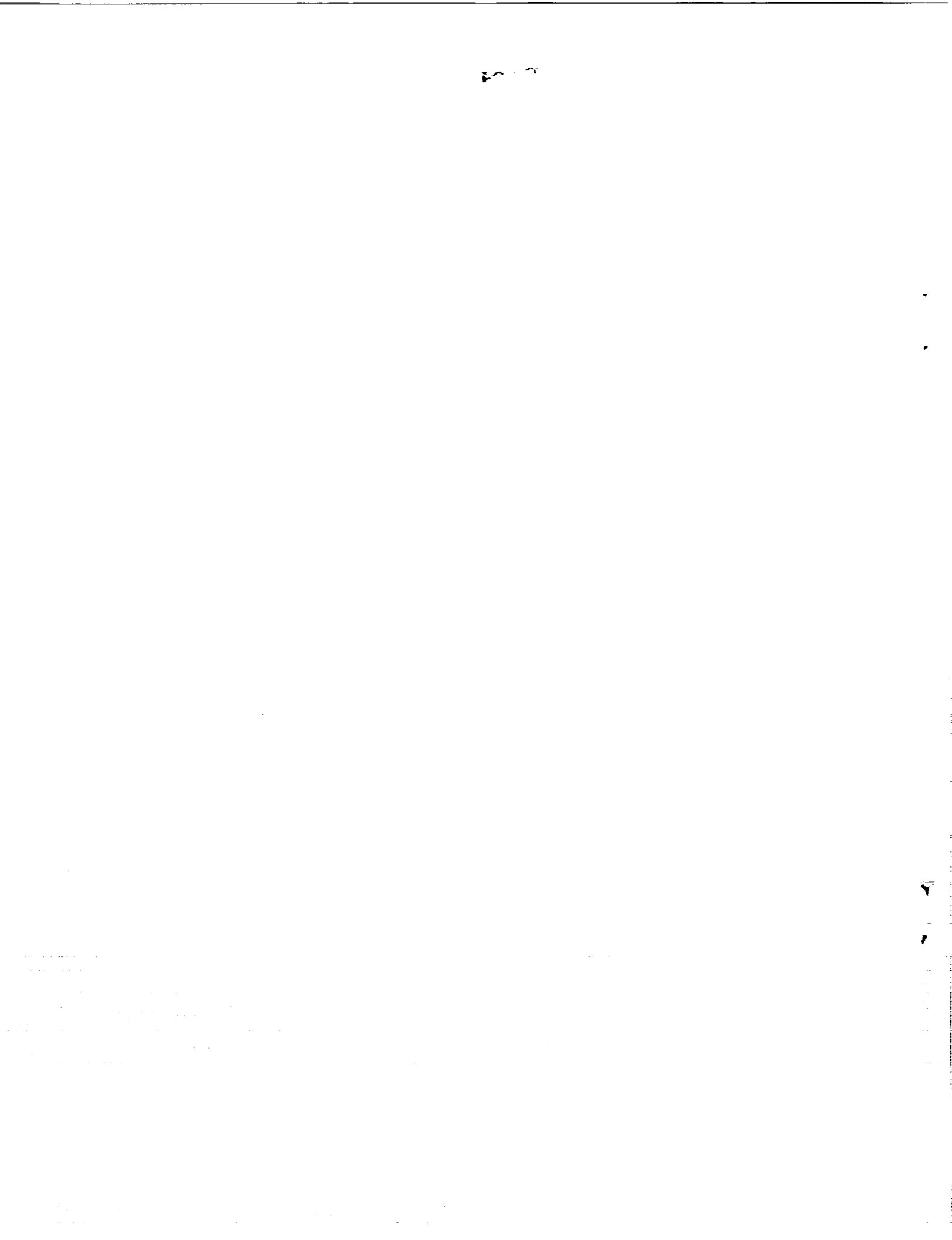
63/18 0329323

January 1991



National Aeronautics and
Space Administration

Langley Research Center
Hampton, Virginia 23665



DETERMINATION OF SHUTTLE ORBITER CENTER OF GRAVITY
FROM FLIGHT MEASUREMENTS

Edwin W. Hinson
ST Systems Corporation
Hampton, VA 23665

John Y. Nicholson
Vigyan Research Associates, Inc.
Hampton, VA 23665

and

Robert C. Blanchard
NASA Langley Research Center
Hampton, VA 23665-5225

Abstract

Flight measurements of pitch, yaw, and roll rates and the resultant rotationally induced linear accelerations during three orbital maneuvers on Shuttle mission STS 61-C have been used to calculate the actual orbiter center-of-gravity location. The calculation technique reduces error due to lack of absolute calibration of the accelerometer measurements and compensates for accelerometer temperature bias and for the effects of gravity gradient. Accuracy of the technique was found to be limited by the nonrandom and asymmetrical distribution of orbiter structural vibration at the accelerometer mounting location. Fourier analysis of the vibration was performed to obtain the power spectral density profiles which show magnitudes in excess of $10^4 \text{ ug}^2/\text{Hz}$ for the actual vibration and over $500 \text{ ug}^2/\text{Hz}$ for the filtered accelerometer measurements. The data from this analysis provide a characterization of the Shuttle acceleration environment which may be useful in future studies related to accelerometer system application and "zero-g" investigations or processes.

Nomenclature

A_i, B_i, C_i	coefficients for HiRAP temperature bias correction ($i = x, z$)
a_{g_i}	acceleration induced by gravity gradient ($i = x, z$)
a_{I_i}	total induced acceleration ($i = x, z$)
a_{M_i}	measured acceleration ($i = x, z$)
a_{r_i}	acceleration induced by rotation ($i = x, y, z$)
a_{T_i}	correction for zero offset and temperature bias ($i = x, z$)
CG	center of gravity
GMT	Greenwich Mean Time
g	acceleration of gravity at sea level (9.806 m/sec ²)
I_{xx}, I_{yy}, I_{zz}	orbiter moments of inertia about X_b, Y_b, Z_b
M_g	orbiter pitching moment induced by gravity gradient
PSD	power spectral density
p, q, r	angular velocities about orbiter X_b, Y_b, Z_b axes
$\ddot{p}, \ddot{q}, \ddot{r}$	angular acceleration about orbiter X_b, Y_b, Z_b axes
\ddot{q}_g	pitch angular acceleration induced by gravity gradient
R	distance from Earth to orbiter
t	time
t_{ref}	reference time for temperature bias correction
t_1, t_2	start and end times for pre-manuever data segment
t_3, t_4	start and end times for manuever data segment
X, Y, Z	HiRAP axes (parallel to orbiter body axes)
X_b, Y_b, Z_b	orbiter body axes

$\bar{x}_i, \bar{y}_i, \bar{z}_i$	offsets of the HiRAP X,Y,Z accelerometer from the orbiter center of gravity along the ith body axis (i = x,y,z)
$\bar{x}_i^{'}, \bar{y}_i^{'}, \bar{z}_i^{'}$	preflight values of \bar{x}_i , \bar{y}_i , and \bar{z}_i
θ	angle between X_b and local vertical
μ_e	Earth gravitational constant ($3.989 \times 10^{14} \text{ m}^3/\text{sec}^2$)
σ	standard deviation
ω	orbital angular velocity

Introduction

Measurement of very low level linear acceleration of the Shuttle Orbiter is one of the principal experiments being conducted as part of the Orbiter Experiments (OEX) Project. The High Resolution Accelerometer Package (HiRAP)¹ has been providing flight measurements since the sixth Shuttle flight on all of the OV-102 Columbia and OV-99 Challenger flights. HiRAP is capable of measurement in the low 10^{-6} g range, which has facilitated the determination of orbiter aerodynamic coefficients and atmospheric density in the hypersonic, rarefied-flow transition region. An even more sensitive accelerometer system, the Orbital Acceleration Research Experiment (OARE)², is ready for installation and will return acceleration measurements in the low 10^{-9} g range. Accurate interpretation of the OARE flight data will require very accurate knowledge of the actual orbiter center-of-gravity location at the time of measurement. This requirement is the stimulus for this analysis of the possibility of orbiter center-of-gravity determination from flight data. Additionally, the technique herein or the results from this study may be of interest relative to attitude guidance and control of large-scale space structures or to experiments sensitive to the orbiter "gravity" environment.

This analysis is formulated on the concept of induced acceleration sensed by a linear accelerometer when the body to which the accelerometer is mounted rotates about its center of gravity. The induced acceleration is proportional to the angular velocity of the body and the offset of the accelerometer axis from the center of gravity. The flight measurements of acceleration for the analysis were obtained from the HiRAP, and the angular velocity data were obtained from the rate gyros on the Aerodynamic Coefficient Identification Package (ACIP), a companion OEX experiment. This report discusses the dedicated orbiter attitude maneuvers for the experiment, the resultant flight data, development of the analysis technique, and results of the analysis.

STS 61-C OEX Attitude Maneuvers

Three attitude maneuvers were performed during the orbital phase of the STS 61-C mission flown by the OV-102 Orbiter (Columbia) in January 1986. These maneuvers were designed to support several OEX experiments, including this analysis of in-flight center-of-gravity determination. The maneuver specifications³ were intended to produce a simple pitch rotation with minimum forces and moments during execution of the maneuver. Figure 1 shows the maneuver geometry with the orbiter initially belly forward and nose down at an angle of 20° with the local vertical. This pre-maneuver attitude was maintained for several minutes by holding a positive pitch rate equal to the orbital angular velocity of 0.0658 deg/sec. The maneuver was initiated with the firing of coarse attitude thrusters to achieve a negative pitch rate of about 0.5 deg/sec, after which the orbiter was allowed to coast in the drift mode (no thruster firings) to the final position with belly aft and nose up at 180° from local vertical. Yaw and roll rates were held to very small values

with $\pm 5^\circ$ tolerances on the target values of 0° for yaw and roll angles. Crew motion, dumps, and vents were inhibited during the maneuvers. ACIP and HiRAP data were recorded for several minutes during the pre-maneuver attitude hold, during the pitch rotation, and for several minutes during the post-maneuver attitude hold.

ACIP Rate Gyro Flight Data

The flight data from the ACIP rate gyros were recorded during the attitude maneuvers and processed postflight at the OEX Data Lab (ODL) at NASA Johnson Space Center (JSC). The processing included calibration corrections for zero bias, temperature, cross-coupling, and other error sources.⁴ The final calibrated data were provided to NASA Langley Research Center (LaRC) in the standard OEX computer-compatible tape (CCT) format at a data sample rate of 112.7 per second. The pitch rate measured by the q-channel rate gyro is shown on figures 2-4 for the three maneuvers and generally conforms to the target specifications with only three noticeable exceptions. The initial overshoot on the pitch rate at the start of maneuver 1 was followed by a very slow adjustment to acquire the final -0.67 deg/sec rate. This adjustment appears to have been obtained by pulsing the vernier thrusters over a 30-second interval. A second deviation occurred during maneuver 3 which shows an initial rate during the pre-maneuver attitude hold which was below the orbital rate, resulting in a slow drift toward local vertical. A correction was made with the vernier thrusters at about $t = 55640$ seconds, which increased the rate substantially above orbital rate and caused a slow drift in the opposite direction. Also in maneuver 3, an unexplained pitch-up, pitch-down perturbation occurred just before the maneuver was started.

HiRAP Accelerometer Flight Data

The HiRAP flight data were also recorded during the maneuvers and processed on the same postflight OEX-CCT as the rate gyro data. However, no postflight calibration of the HiRAP data was performed at the ODL, and the data received at LaRC were in the form of raw counts from the HiRAP data electronics. The counts from the X- and Z-axis accelerometers were converted to units of 10^{-6} g and plotted (relative to the initial value) in figures 5-10. A steep negative slope caused by a large temperature-dependent bias is clearly evident in the figures. The actual accelerations, both X- and Z-channels, are known to be small, on the order of 10^{-6} g, during the pre-maneuver hold period. During the maneuver, the theoretical induced acceleration in the X-channel based on the measured pitch rate is about 43×10^{-6} g for maneuver 1 and about 21×10^{-6} g for maneuvers 2 and 3. The corresponding values for the Z-channel are -28×10^{-6} g and -13×10^{-6} g. These induced accelerations can be seen in the plots even in the presence of the temperature slope and large noise levels.

Rotationally Induced Acceleration

A linear accelerometer mounted on a translating, rotating body at some distance from the body CG will have an output proportional to the algebraic sum of the projections onto the accelerometer axis of the linear acceleration of the body, the rotationally induced acceleration of the proof mass, and the gravity-gradient-induced acceleration of the proof mass. Previous analysis of the HiRAP data⁵ involved the extraction of the linear contributions which required an analytical correction for rotation based on the ACIP rate gyro

measurements of rotation rates. The equations for rotationally induced acceleration⁶ for the three HiRAP axes are

$$a_{r_x} = -(q^2 + r^2) \bar{X}_x + (pq - \dot{r}) \bar{Y}_x + (pr + \dot{q}) \bar{Z}_x$$

$$a_{r_y} = (pq + \dot{r}) \bar{X}_y + (p^2 + r^2) \bar{Y}_y + (qr - \dot{p}) \bar{Z}_y$$

$$a_{r_z} = (pr - \dot{q}) \bar{X}_z + (qr + \dot{p}) \bar{Y}_z + (p^2 + q^2) \bar{Z}_z$$

where a_{r_i} , $i = x, y, z$, are the total rotationally induced accelerations; p , q , and r are angular velocities about X_b , Y_b , and Z_b ; and \bar{X}_i , \bar{Y}_i , \bar{Z}_i are offsets of the X , Y , and Z accelerometers from the CG along the i th body axis. The offsets for the X - and Z -channel accelerometers are shown two dimensionally ($i = x, z$) in figure 11.

An in-depth analysis of the relative contribution of the various terms, based upon STS 61-C attitude maneuver data, was performed to aid simplification of these equations. The Y -axis was omitted from consideration because the orbiter CG and the Y -channel accelerometer are both very close to the lateral plane of symmetry so that the anticipated uncertainty in determination of the offset is of the same order of magnitude as the offset. The ACIP on STS 61-C had an inoperative p -channel rate gyro; however, average values of p were determined from the postflight attitude and trajectory history⁷ for STS 61-C. These values are shown for comparison with the average ACIP q and r values in tables 1 and 2 for the pre-maneuver and maneuver segments, respectively. Retaining only the terms which produce accelerations greater than $0.1 \times 10^{-6} g$ and assuming that $\dot{p} = \dot{q} = \dot{r} = 0$ reduces the equations to

$$a_{r_x} = - (q^2 + r^2) \bar{X}_x$$

$$a_{r_z} = q^2 \bar{Z}_z$$

Gravity Gradient Effects

The substantial distance (3.7 m) between the CG and the HiRAP mounting location contributes to non-negligible gravity-gradient-induced acceleration in both X- and Z-channels. This acceleration is given for a circular orbit (valid assumption for STS 61-C) by

$$a_{g_x} = 2 \omega^2 (\bar{x}'_x^2 + \bar{z}'_z^2)^{1/2} \left| \cos \theta \cos (\theta + \tan^{-1} \frac{\bar{z}'_z}{\bar{x}'_x}) \right|$$

$$a_{g_z} = -2 \omega^2 (\bar{x}'_x^2 + \bar{z}'_z^2)^{1/2} \left| \sin \theta \cos (\theta + \tan^{-1} \frac{\bar{z}'_z}{\bar{x}'_x}) \right|$$

where ω is the orbital angular velocity (≈ 0.0658 deg/sec for STS 61-C), θ is the angle between the X_b axis and local vertical, and \bar{x}'_x and \bar{z}'_z refer to pre-flight values. The maximum value of a_{g_x} is 0.91×10^{-6} g, which occurs at $\theta = -16.7^\circ$ and 163.3° , and the maximum magnitude of a_{g_z} occurs at $\theta = -61.7^\circ$ and 118.3° with $a_{g_z} = -0.7 \times 10^{-6}$ g. Since each a_{g_i} is a small contribution (5 percent or less) to the total measured acceleration, the use of \bar{x}'_x and \bar{z}'_z introduces negligible error.

The gravity gradient torque exerted on the orbiter during the OEX maneuvers was primarily about the Y_b axis and is given by

$$M_g = \frac{3 \mu_e}{R^3} (I_{xx} - I_{zz}) \sin \theta \cos \theta$$

The induced angular acceleration is then

$$\dot{\varphi}_g = \frac{M_g}{I_{yy}} = \frac{3 \mu_e}{R^3 I_{yy}} (I_{xx} - I_{zz}) \sin \theta \cos \theta$$

which reduces to approximately

$$\ddot{q}_g = -3.6 \times 10^{-6} \sin \theta \cos \theta \text{ (sec}^{-2}\text{)}$$

for the STS 61-C orbiter mass properties and orbital altitude. This angular acceleration tends to stabilize the orbiter X_b axis along the local vertical, either nose up or nose down. The maximum absolute value of \ddot{q}_g , $1.8 \times 10^{-6} \text{ sec}^{-2}$, occurs at $\theta = \pm 45^\circ$ and $\pm 135^\circ$ and induces an X-channel linear acceleration of about $\pm 0.36 \times 10^{-6} \text{ g}$ and a Z-channel value of about $\pm 0.56 \times 10^{-6} \text{ g}$. The presence of this effect is clearly evident in figure 12, which shows the maneuver 3 ACIP pitch rate history from $\theta = 0^\circ$ to 180° compared with the theoretical pitch rate obtained by integrating the equation for \ddot{q}_g .

Aerodynamic Forces and Moments

The STS 61-C mission was flown during minimum solar activity when the atmospheric density was minimum at the 61-C orbital altitude. The expected aerodynamic acceleration for this condition, based on the latest orbiter flight-derived free-molecule-flow aerodynamic coefficients⁸, is less than $0.1 \times 10^{-6} \text{ g}$ and is considered to be negligible. The maximum aerodynamic pitching moment (from C. Cooke and others at Charles Stark Draper Laboratory, study of Shuttle experiment acquisition, tracking and pointing for Jet Propulsion Laboratory) produces a \ddot{q} of $2.3 \times 10^{-7} \text{ sec}^{-2}$, which would induce negligible linear accelerations of $0.05 \times 10^{-6} \text{ g}$ in the X-channel and $0.07 \times 10^{-6} \text{ g}$ in the Z-channel.

HiRAP Zero Offset and Temperature Bias

The outputs of the HiRAP accelerometer are temperature dependent and must be calibrated accordingly for each data set to provide the desired absolute measurement accuracy. This calibration is normally accomplished through analysis of flight data from an on-orbit calibration sequence.⁵ The zero bias is established for a reference point, t_{ref} , and the temperature bias slope in

integrated over the subsequent measurement interval based on measurements from accelerometer-mounted thermocouples. For a linear variation in temperature with time, this correction is equal to

$$a_{T_x} = A_x + B_x (t - t_{ref}) + C_x (t - t_{ref})^2$$

$$a_{T_z} = A_z + B_z (t - t_{ref}) + C_z (t - t_{ref})^2$$

which is the form used in this analysis. However, no separate calibration analysis was performed to solve for the coefficients A_i , B_i , and C_i ; rather, their solution was obtained simultaneously with the solution for the CG offsets.

Solution for CG Offsets

From the foregoing considerations, the total induced accelerations from the significant sources are

$$a_{I_x} = - (q^2 + r^2) \bar{X}_x + a_{g_x} + \dot{a}_g \bar{Z}'_z$$

$$a_{I_z} = q^2 \bar{Z}_z + a_{g_z} + \dot{a}_g \bar{X}'_z$$

The i th accelerometer flight measurement is then equal to these induced accelerations plus the reference zero offset and temperature bias at time t_i .

$$a_{M_{x_i}} = - (q_i^2 + r_i^2) \bar{X}_x + a_{g_{x_i}} + \dot{a}_{g_i} \bar{Z}'_x + A_x + B_x (t_i - t_{ref}) + C_x (t_i - t_{ref})^2$$

$$a_{M_{z_i}} = q_i^2 \bar{Z}_z + a_{g_{x_i}} - \dot{a}_{g_i} \bar{X}'_z + A_z + B_z (t_i - t_{ref}) + C_z (t_i - t_{ref})^2$$

These equations were used with a least squares routine with matrix inversion to solve for the four unknowns in each equation; \bar{X}_x , A_x , B_x , and C_x for the X-channel and \bar{Z}_z , A_z , B_z , and C_z for the Z-channel; while

minimizing the difference between the measured acceleration on the left and the calculated acceleration on the right. The data sample used in this solution includes a period during the pre-maneuver attitude hold and an interval during the maneuver. The solution is equivalent to solving for the CG offsets based on the change in induced acceleration for a given change in the pitch angular velocity between the two periods, an approach which is forced by the lack of absolute calibration of the measured accelerations.

Selection of Data Segments for Analysis

Figure 13 shows graphically the definition of the two data segments used for each maneuver in the CG offset calculations. The pre-maneuver hold segment from t_1 to t_2 was selected to be free from major unmodeled perturbations and to end prior to the thruster firing which initiated the maneuvers. The maneuver segment from t_3 to t_4 was started after the thruster firing accelerations had damped to a negligible level and contained no major unmodeled perturbations. The selected segments for the three maneuvers are listed in table 3 with the values for t_{ref} which were taken to be the approximate time of maneuver initiation. Each of these segments is approximately 100 seconds long and contains about 11,200 measurements for a total of about 22,400 for each maneuver.

CG Offset Solutions

Solutions were obtained for \bar{X}_X and \bar{Z}_Z for the three maneuvers using the data segments defined in table 3 and also for a group of restricted data sets. The restricted data sets were defined by applying the criterion that any measurement whose residual (measured acceleration minus calculated acceleration) in the unrestricted solution exceeds $n\sigma$ is deleted from the data set. A value of n greater than 7 produces essentially an unrestricted data

set, while decreasing values of n produce data sets which are increasingly more restricted to the central measurements. The CG offsets obtained for the unrestricted data and for the sets with $n = 6, 5, 4, 3$, and 2 are listed in table 4 and also shown in figure 14 compared with the pre-flight values.

Significant variations in \bar{X}_x and \bar{Z}_z are present in the solutions from maneuver to maneuver and also across the restricted solutions for a given maneuver. These results show a strong sensitivity to the distribution of "noise" in the data, which indicates violation of the assumption of random normal distribution of noise. The distributions of residuals over the pre-maneuver and maneuver segments are shown for the unrestricted solutions in figures 15-20 with the theoretical normal distribution curve shown for comparison. Some significant departures from random normal are seen in these distributions, both in the central values which would account for the variation in the CG offset solution from maneuver to maneuver and in the outlying values which would account for the variations in the restricted solutions. Without exception, the quality of fit of the flight data obtained in each solution varies between the two segments with the most pronounced difference occurring in the maneuver 3 X-axis solution, figure 17, for which the far better fit of the maneuver segment is evident in the high concentration of central values. In general, these distributions show much larger than expected (based on the random normal assumption) concentrations of outlying values above 3σ which are typically non-symmetrical about the mean. Further, the outlying values are not randomly distributed over the data segment but occur as one or more large peaks. For example, the maneuver 3 Z-axis pre-maneuver segment contains 43 measurements whose residuals exceed 4σ , only 3 of which are negative, with 9 positive values in one single peak and 30 positive values in a second peak. A

similar situation exists with the maneuver segment for this case which has 55 measurements above 4σ , of which 46 are positive and contained within four peaks. The probability of occurrence of values above 4σ for a random normal distribution is only 6×10^{-5} , or one value in the 22,400 measurements compared with a total of 98 for this case.

Analysis of Noise/Vibration Effects

The noise level on the rate gyro data is about 4 to 6 percent of the measured signal and appears to be random. However, the noise level in the accelerometer data is of the same order as the rotationally induced acceleration and frequently exceeds $\pm 50 \times 10^{-6}$ g. Figure 21 shows the X-channel accelerometer output for an expanded time scale which depicts the variations more clearly than does figure 5. The signal does not exhibit the characteristics of random noise but rather reflects the expected orbiter structural vibration characteristics; e.g., a composite waveform produced by several vibration sources such as motors, pumps, and directional antenna systems.

A fast Fourier transform routine was used to determine the power spectral density in the accelerometer output for each of the data segments as shown in figures 22-27. The sample size for this routine was 8192 (²¹³), reduced from the segment size of 11,200, and therefore covers only 73 seconds of the 100-second segments. Noticeable differences between the spectra are seen when comparing the pre-maneuver and maneuver segments for maneuvers 1 and 3 in both X- and Z-channels. For example, the pre-maneuver sequence during maneuver 3 for the X-channel (figure 24(a)) shows much lower amplitudes below 2 Hz than the maneuver segment in figure 24(b), while the opposite is true of maneuver 1 in figures 22(a) and (b). More dramatic differences are seen in the Z-channel spectra for maneuvers 1 and 3 where large amplitude spikes are seen in one

segment (figures 25(a) and 27(b)) but not in the other segment. Also, the orbiter structural resonance near 5 Hz (first longitudinal bending mode) is stronger in the Z-channel. Given the changes that frequently occur between the pre-maneuver and maneuver segments, significant changes could be expected even during the span of a single segment. Such changes could certainly alter the degree to which the vibration signal is randomized and thereby affect the CG offset solution. A model of the vibration environment for the maneuver 3, Z-axis case was developed from its component spectrum and was used to generate a simulated vibration signal which was superimposed on the theoretical output of HiRAP for the target orbiter rotation rates. Sine waves spaced at 0.0138 Hz from 0.1 to 3.0 Hz with amplitudes consistent with the component spectra were started at zero phase angle 50,000 sec prior to tref in order to randomize the composite signal. The simulated HiRAP data were input to the CG offset solution routine which produced the residual distribution shown in figure 28. This distribution shows more symmetry and a higher concentration near the mean when compared with the distributions from the flight data solutions.

Unfiltered Orbiter Vibration

The power spectral density profiles obtained from the HiRAP data contain few clues, if any, to the nature and source of the vibrations which would lead to improvement of the CG solutions. The possibility that the low-frequency 0 to 3 Hz spectrum could be in part due to beating of closely spaced frequencies above 5 Hz led to the generation of power spectral density profiles which were corrected for the 43 db per decade rolloff of HiRAP between 2 and 20 Hz. These spectra are shown in figures 29-34. The first longitudinal bending

mode resonance near 5 Hz is more pronounced and the large directional antenna "dither" motion is seen at 17 Hz. Higher frequency components in the range of 5 to 15 Hz are much stronger in the Z-channel as compared with the X-channel. No obvious correlation between the higher frequencies and the lower frequencies is present. These data indicate, within the limits of the fast Fourier transform technique⁹, the expected level of vibrationally induced acceleration at the HiRAP mounting location, even during a so-called "quiet" period, which would bear on any "zero-g" investigation or process.

Conclusions

The technique for determination of the orbiter center of gravity from flight measurements as described herein produces results which are reasonably accurate considering the complex acceleration environment in which the measurements were obtained. The orbiter structural vibration produces a complex acceleration waveform which is composed of a number of different frequencies generated by various mechanical subsystems. The operating schedule for the subsystems varies as does the degree to which the resultant waveform is randomized. The occasional in-phase amplitude peaks are not random over the relatively short time segments used in this analysis. Consequently, the center-of-gravity solution is sensitive to the choice of data segment length and position and also to any statistical culling procedure. The observed variation in the solutions is due primarily to variations in the sample distribution and not to measurement errors or first-order errors in the temperature bias model; therefore, any improvement in measurement accuracy or temperature model would not improve the solution. Such improvement would require more sophisticated analytical and/or statistical methods beyond the scope of this study. The improved low-pass filter on the OARE will further

attenuate the vibration signals and the digital filtering techniques to be applied during the processing may further reduce the vibration-induced errors in the center-of-gravity solution.

References

¹Blanchard, R. C. and Rutherford, J. F., "Shuttle Orbiter High Resolution Accelerometer Package Experiment: Preliminary Flight Results," Journal of Spacecraft and Rockets, Vol. 22, No. 4, July-August 1985, pp. 474-480.

²Blanchard, R. C., et al., "Orbital Acceleration Research Experiment," Journal of Spacecraft and Rockets, Vol. 24, No. 6, November-December 1987, pp. 504-511.

³Detailed Test Objective 0902, JSC-16725, Rev. G., November 1985.

⁴Kintzer, M. J., "Aerodynamic Coefficient Identification Package (ACIP) Calibration Report - Calibration 2, January 1983," NASA Report No. JSC-19362 prepared by Lockheed Engineering and Management Services Co., Nov. 1983.

⁵Thompson, J. M., Russell, J. W., and Blanchard, R. C., "Methods for Extracting Aerodynamic Acceleration from Orbiter High Resolution Accelerometer Package Flight Data," AIAA Paper 87-2365, August 1987.

⁶Wagner, W. E. and Serold, A. C., "Formulation on Statistical Trajectory Estimation Programs," NASA CR-1482, January 1970.

⁷Cooper, D. H. and Parker, K. C., "STS-61C Final Report: On-Orbit Post-Flight Reconstruction," prepared for NASA/JSC by TRW Defense Systems Group (TRW 47467-H004-UX-00), March 1986.

⁸Blanchard, R. C., Hinson, E. W., and Nicholson, J. Y., "Shuttle High Resolution Accelerometer Package Experiment Results: Atmospheric Density Measurements Between 60 and 160 km," Journal of Spacecraft and Rockets, Vol. 26, No. 3, May-June 1989, pp. 173-180.

⁹Southworth, R., "Autocorrelation and Spectral Analysis," in Mathematical Methods For Digital Computers, New York, J. Wiley and Sons, 1962, pp. 213-220.

Table 1 Average rotational rates during pre-maneuver hold (deg/sec)

	<u>Maneuver 1</u>	<u>Maneuver 2</u>	<u>Maneuver 3</u>
p	.001	-.0013	.002
q	.06	.06	.1
r	-.014	-.013	-.011

Table 2 Average rotational rates during maneuvers (deg/sec)

	<u>Maneuver 1</u>	<u>Maneuver 2</u>	<u>Maneuver 3</u>
p	-.01	.018	.008
q	-.67	-.47	-.47
r	-.029	.0036	-.0014

Table 3 Data Segments (GMT seconds)

	<u>Maneuver 1</u>	<u>Maneuver 2</u>	<u>Maneuver 3</u>
t_1	31560	60068	55675
t_2	31660	60168	55775
t_{REF}	31700	60177	55805
t_3	31730	60210	55840
t_4	31830	60310	55940

Table 4 CG offsets obtained for various data restrictions.

<u>Restrictions</u>	\bar{x}_x (pre-flight value = -3.07 m)			Mean \pm deviation, m
	Maneuver 1, m	Maneuver 2, m	Maneuver 3, m	
none	-2.932	-3.112	-3.077	-3.040 \pm .078
6 σ	-2.956	-3.132	-3.205	-3.098 \pm .105
5 σ	-2.968	-3.132	-3.285	-3.128 \pm .129
4 σ	-2.982	-3.123	-3.277	-3.127 \pm .120
3 σ	-3.019	-3.118	-3.103	-3.080 \pm .044
2 σ	-3.142	-2.987	-3.063	-3.064 \pm .063
<u>Restrictions</u>	\bar{z}_z (pre-flight value = 2.021 m)			Mean \pm deviation, m
	Maneuver 1, m	Maneuver 2, m	Maneuver 3, m	
none	1.986	1.894	2.145	2.008 \pm .104
6 σ	2.058	1.971	2.145	2.058 \pm .071
5 σ	2.030	1.956	2.107	2.031 \pm .062
4 σ	2.004	1.942	2.070	2.005 \pm .052
3 σ	1.953	1.933	2.125	2.004 \pm .086
2 σ	1.974	1.931	2.118	2.008 \pm .080

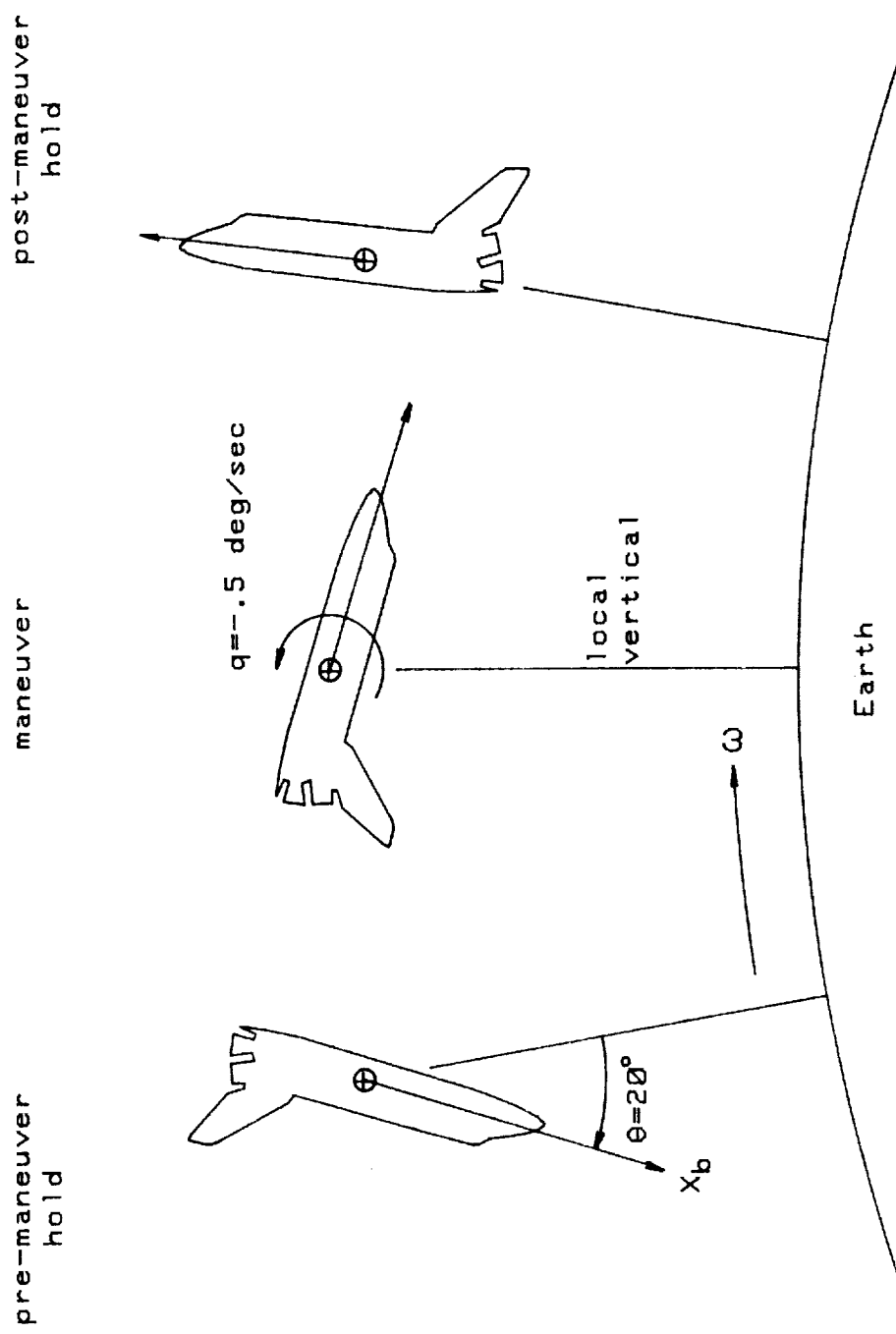


Figure 1. STS-61C OEX attitude maneuver geometry.

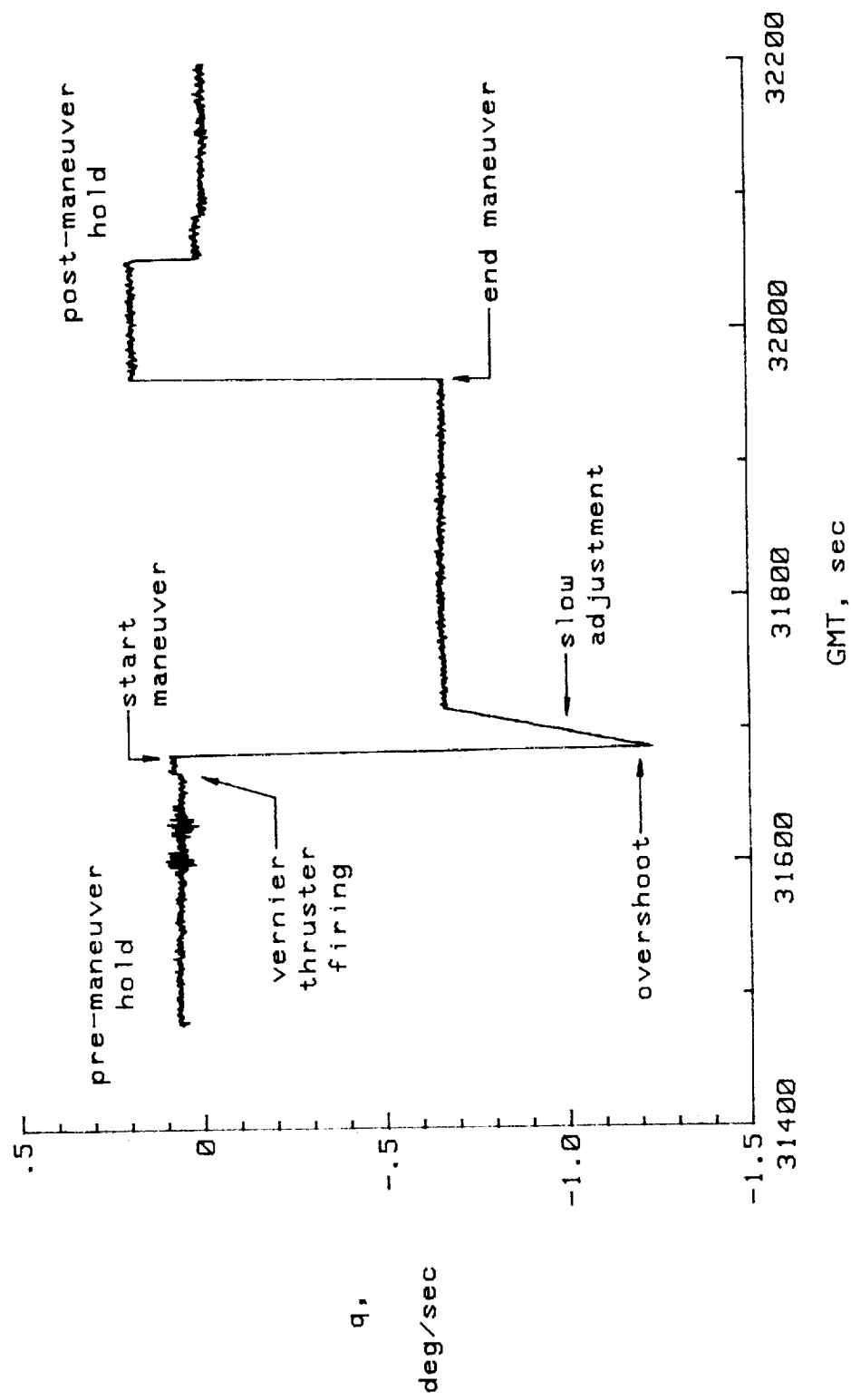


Figure 2. Angular rate about orbiter Y-axis, maneuver 1.

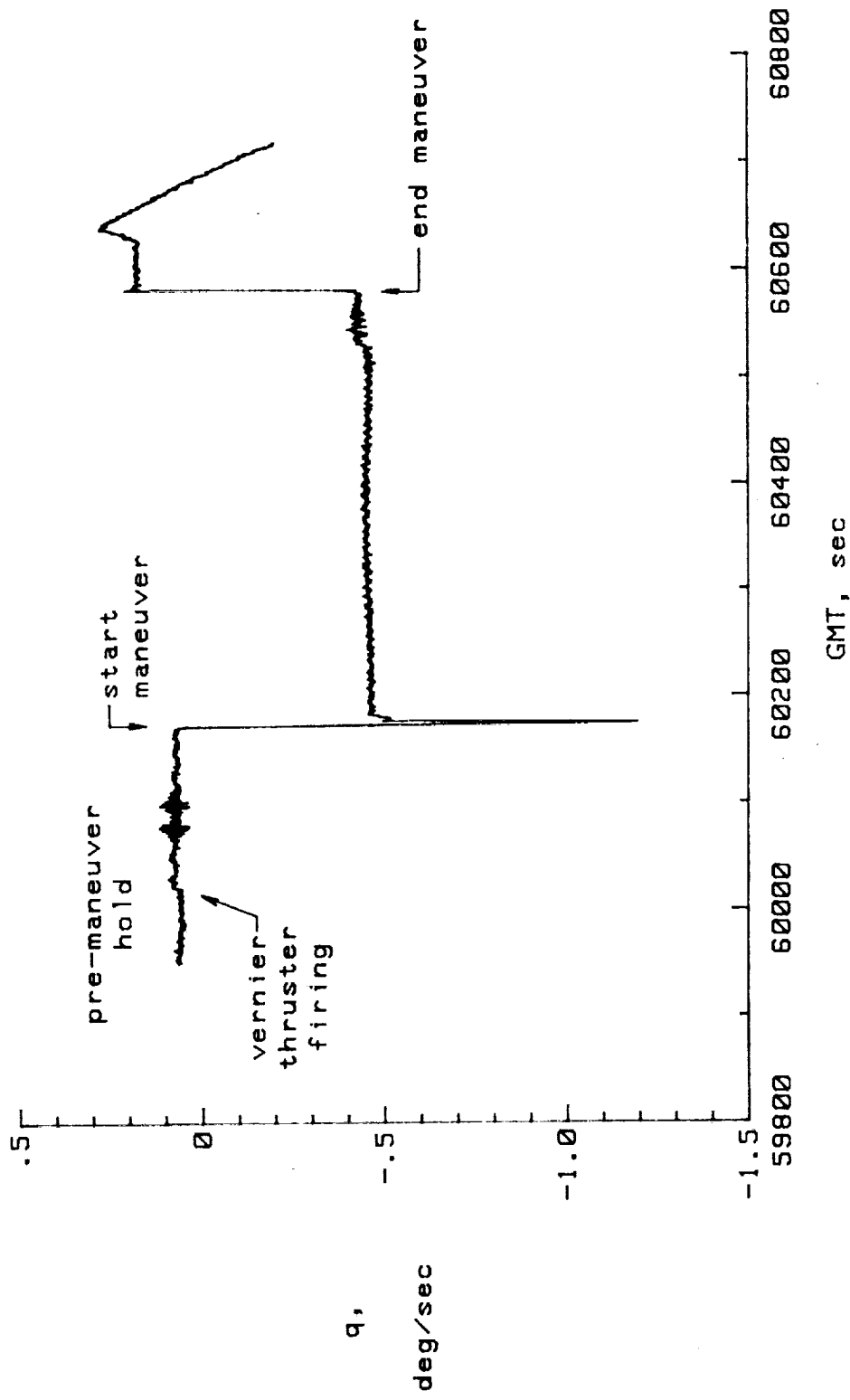


Figure 3. Angular rate about orbiter Y-axis, maneuver 2.

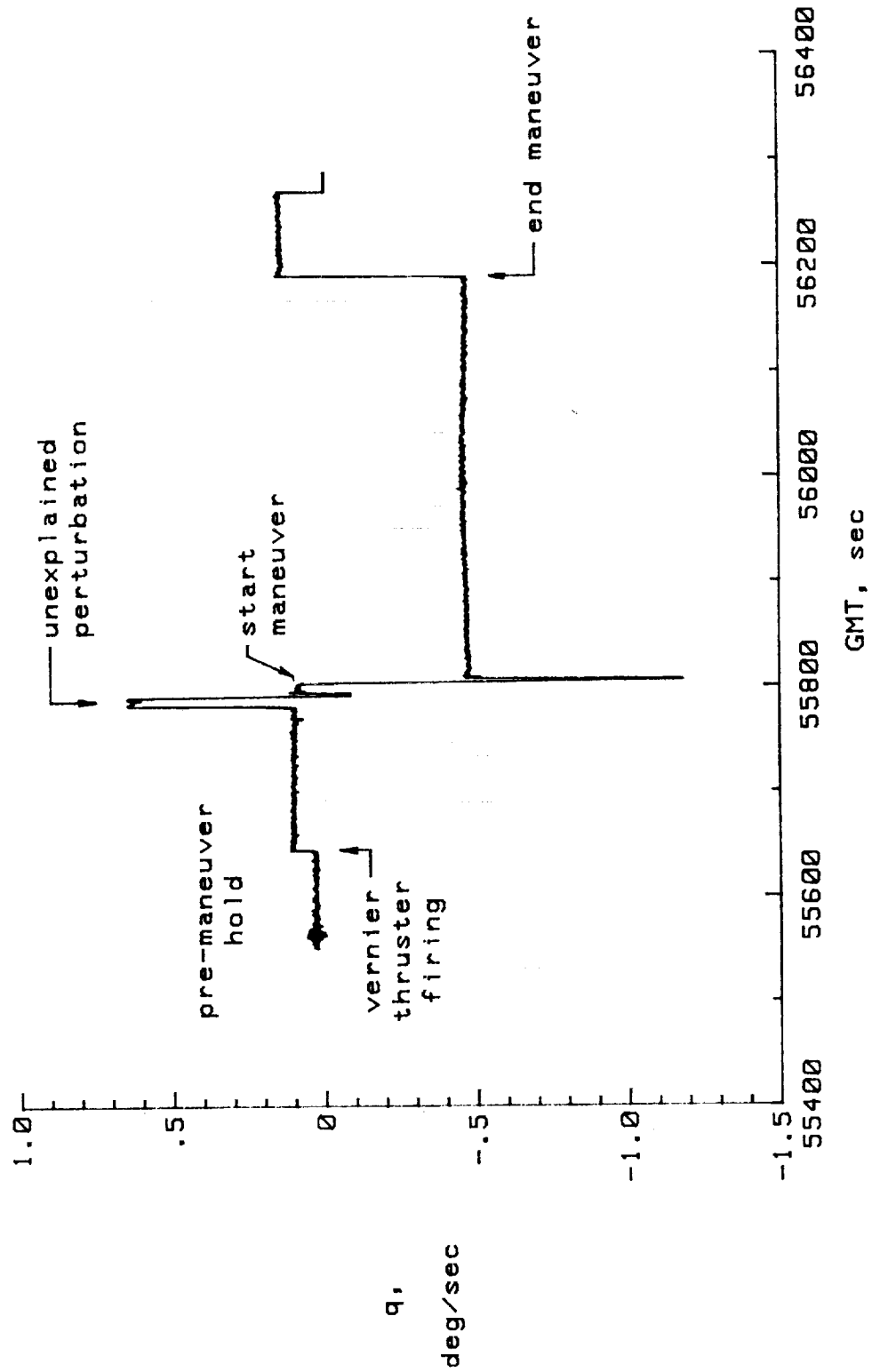


Figure 4. Angular rate about orbiter Y-axis, maneuver 3.

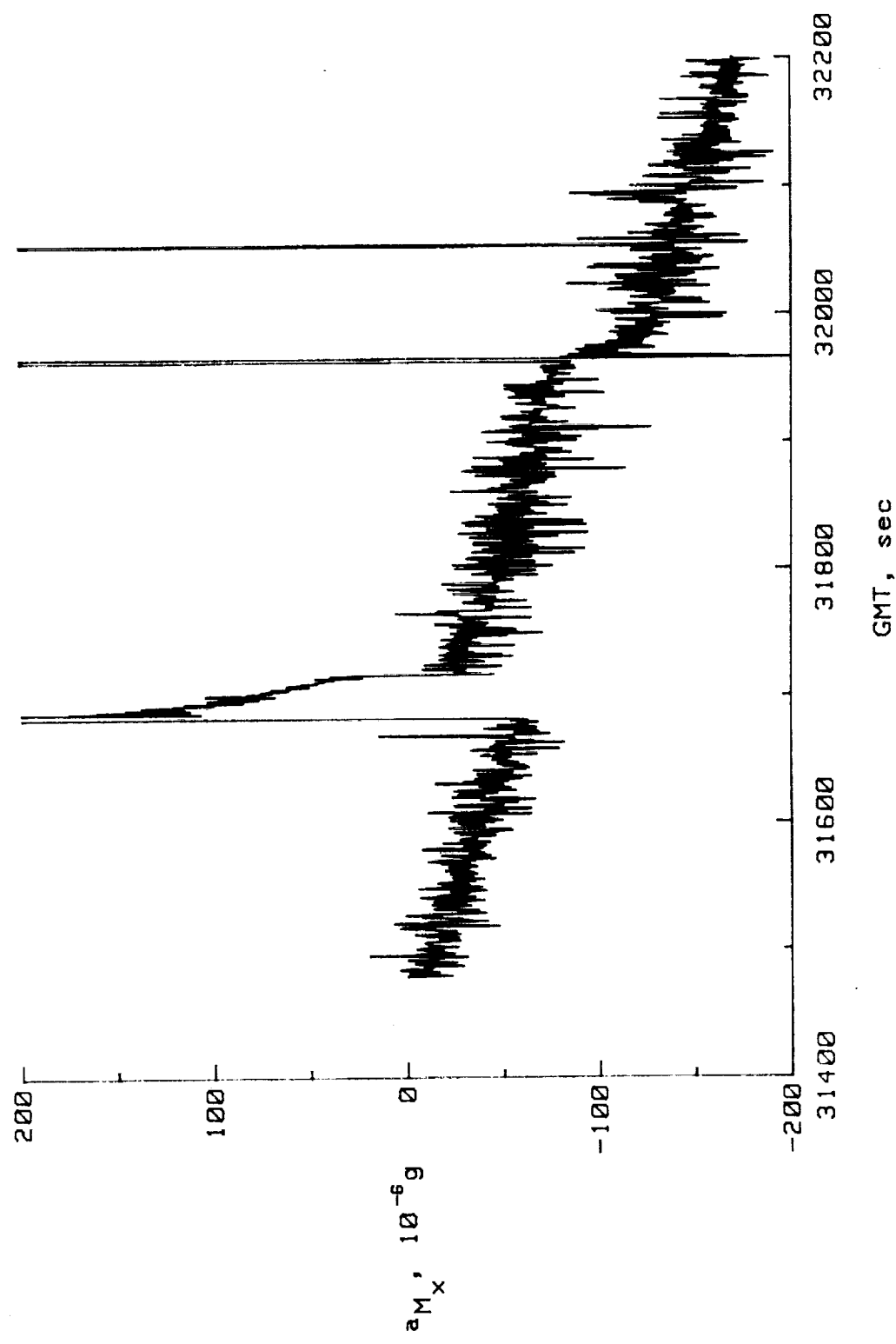


Figure 5. HiRAP X-channel relative output, maneuver 1.

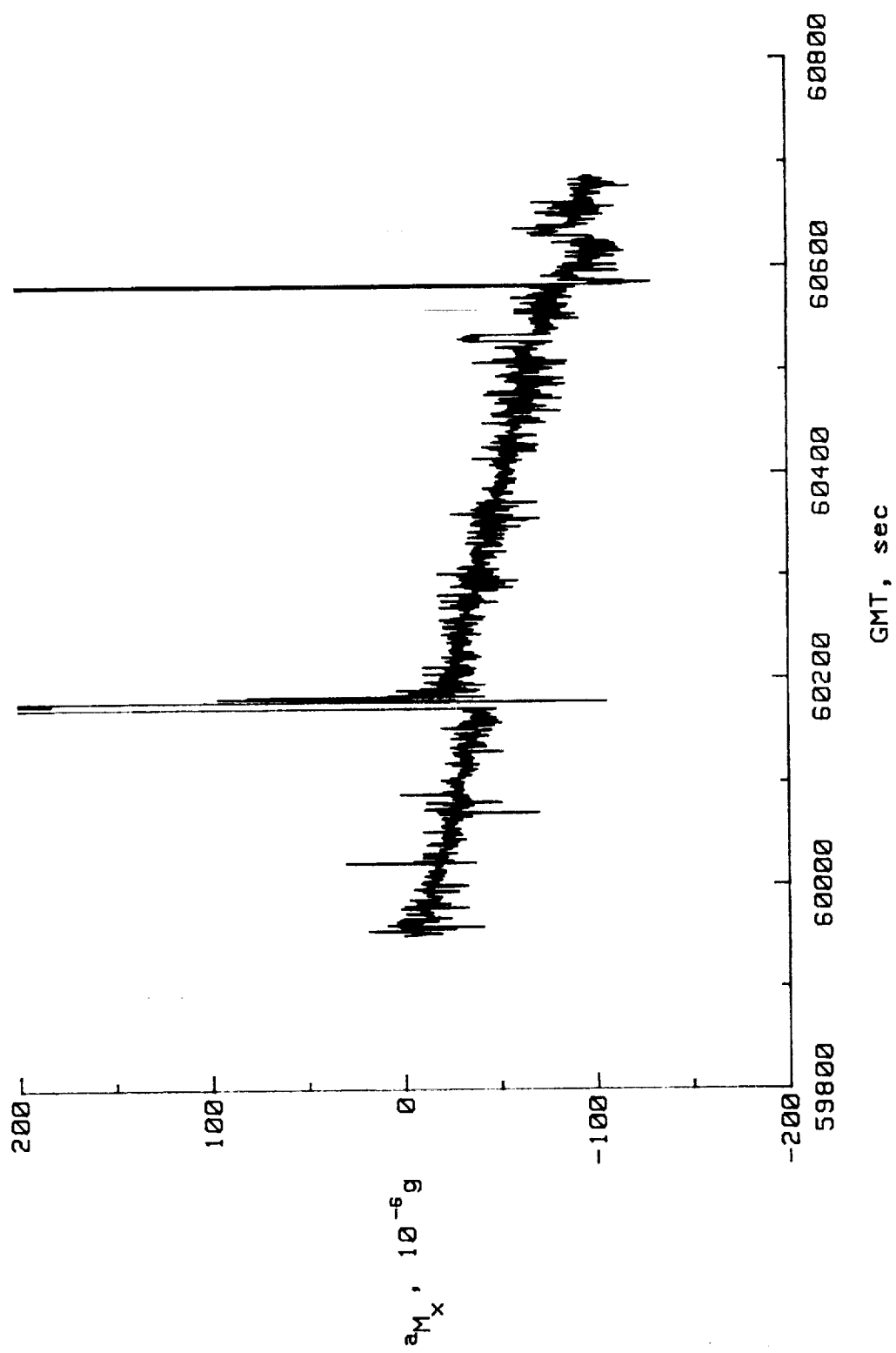


Figure 6. HIRAP X-channel relative output, maneuver 2.

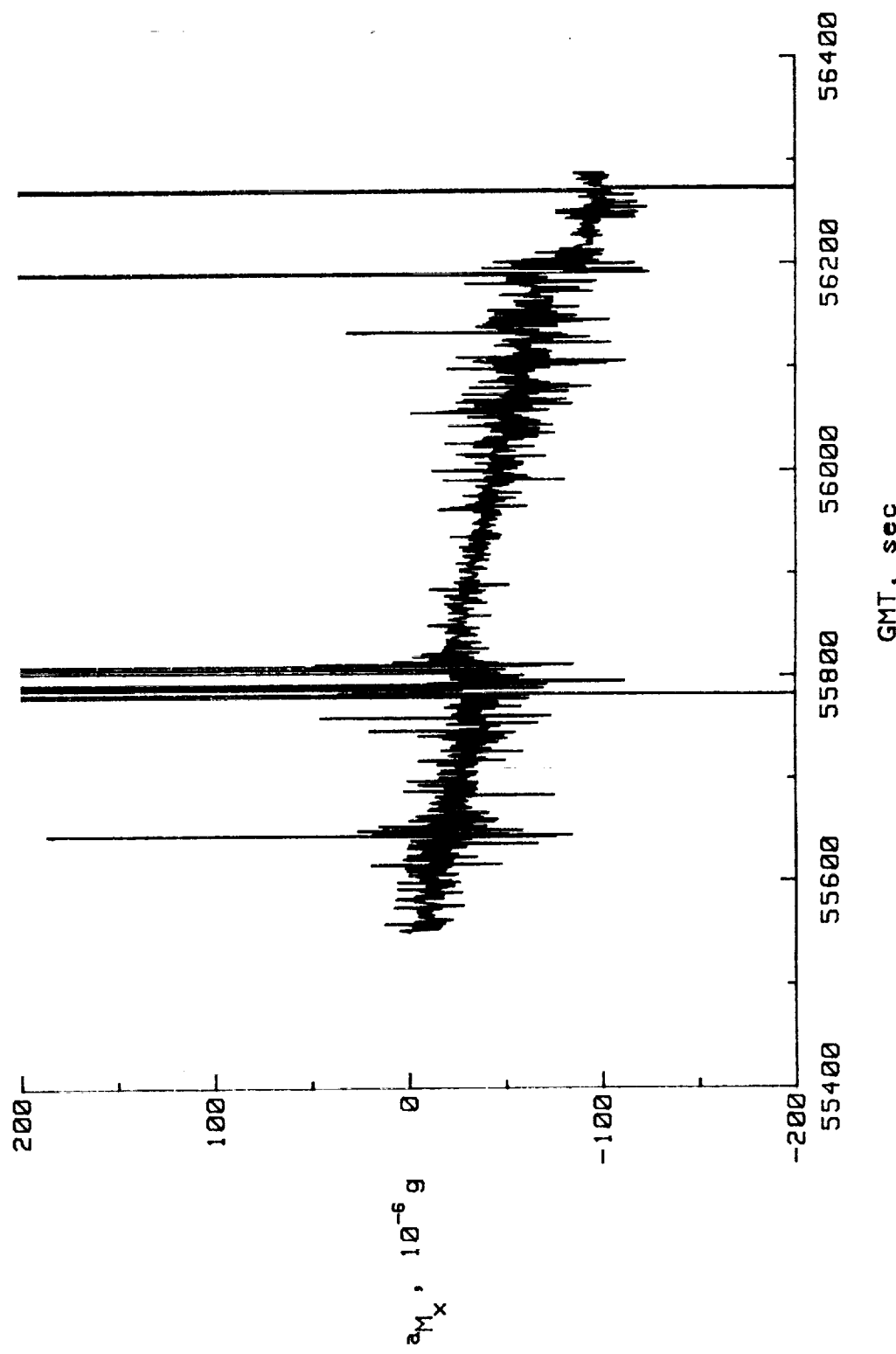


Figure 7. HiRAP X-channel relative output, maneuver 3.

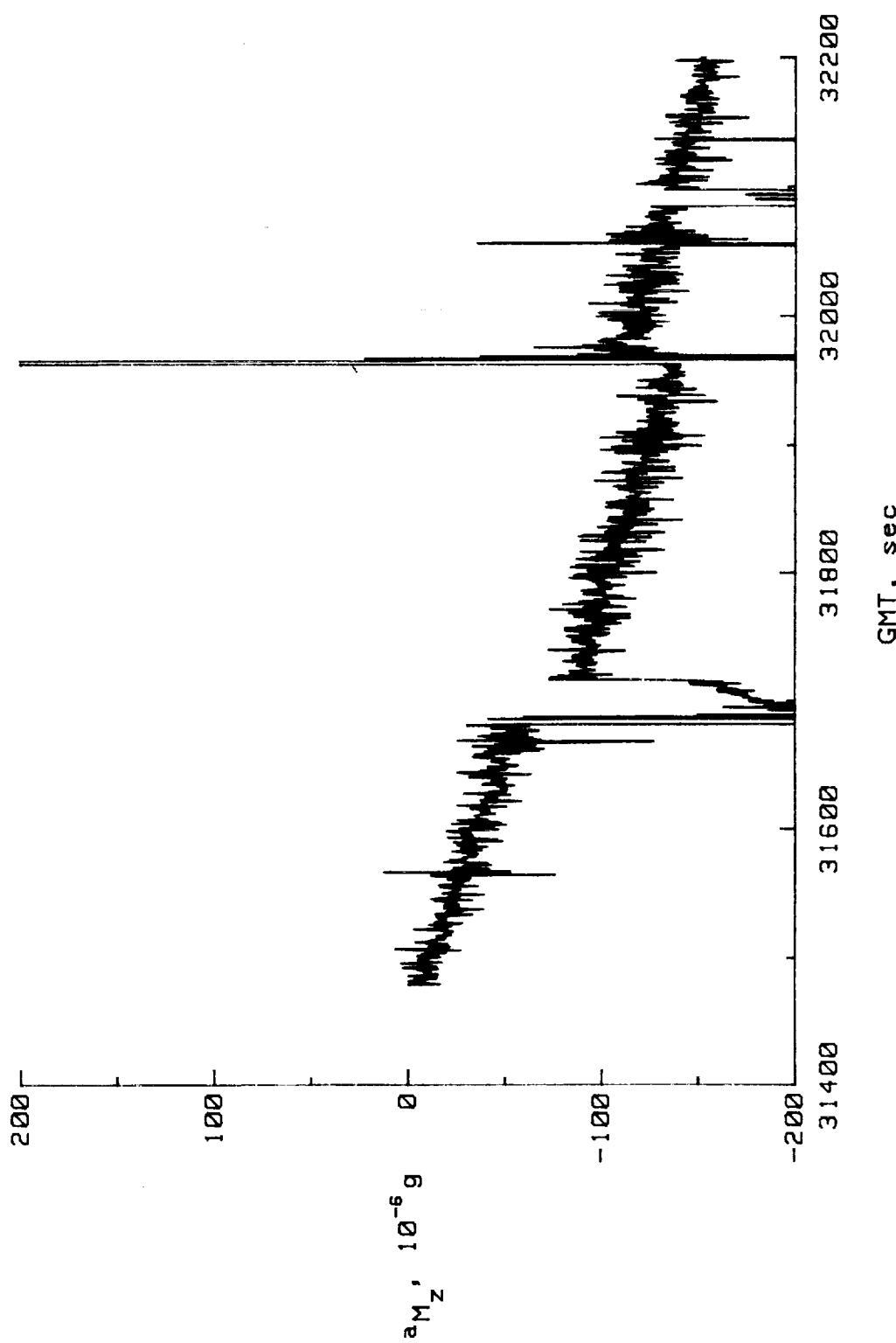


Figure 8. HIRAP Z-channel relative output, maneuver 1.

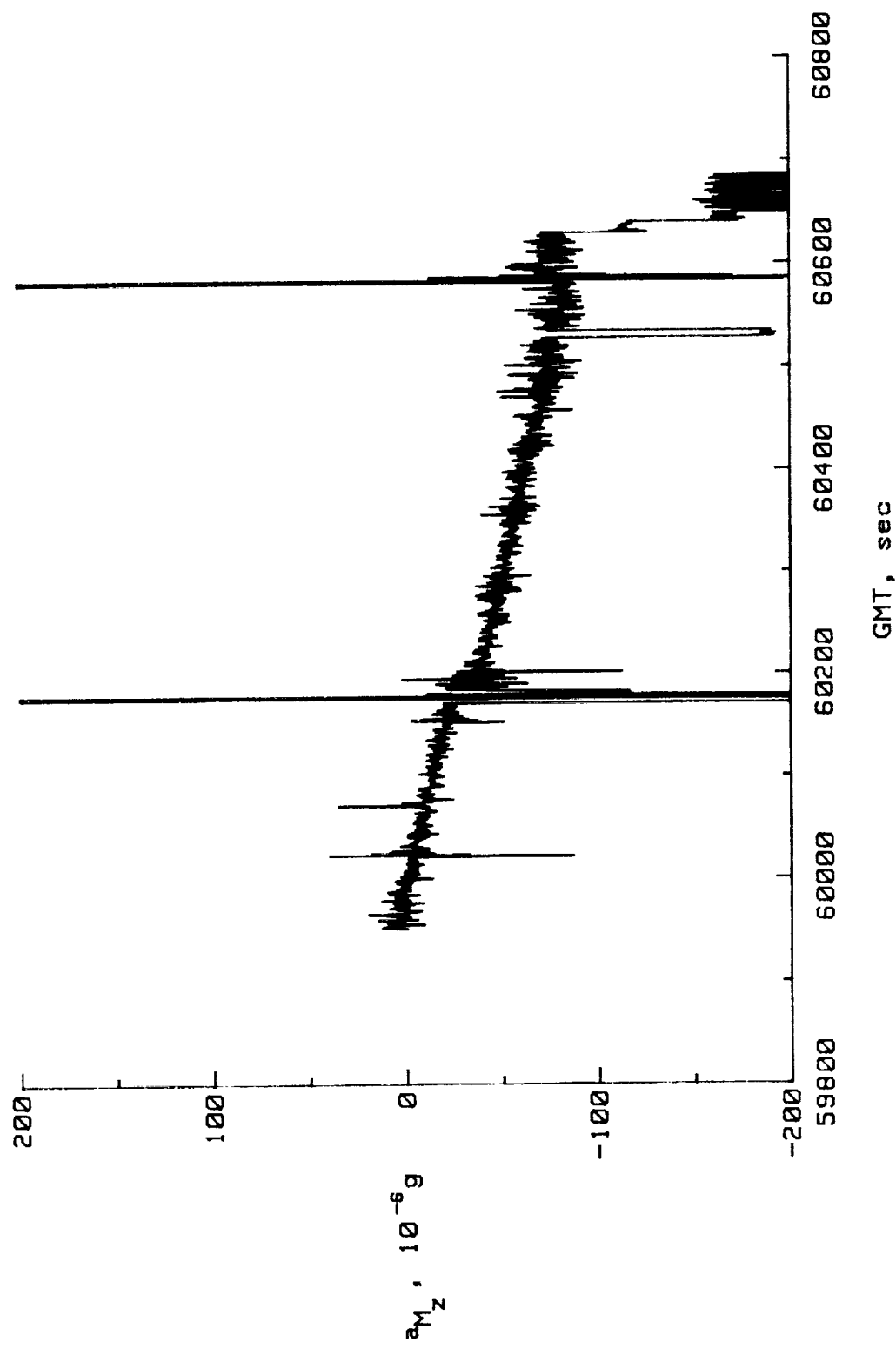


Figure 9. HIRAP Z-channel relative output, maneuver 2.

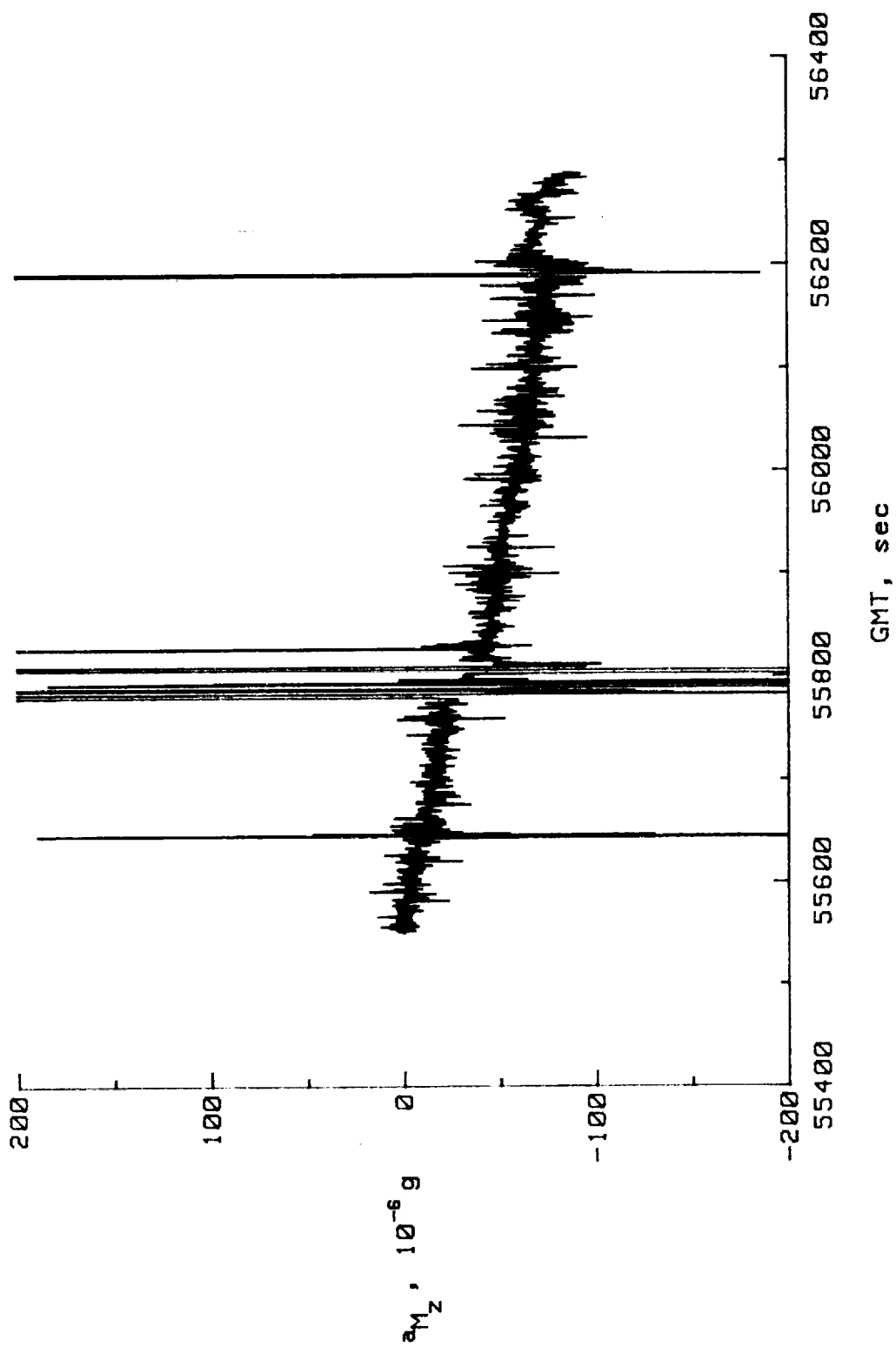


Figure 10. HIRAP Z-channel relative output, maneuver 3.

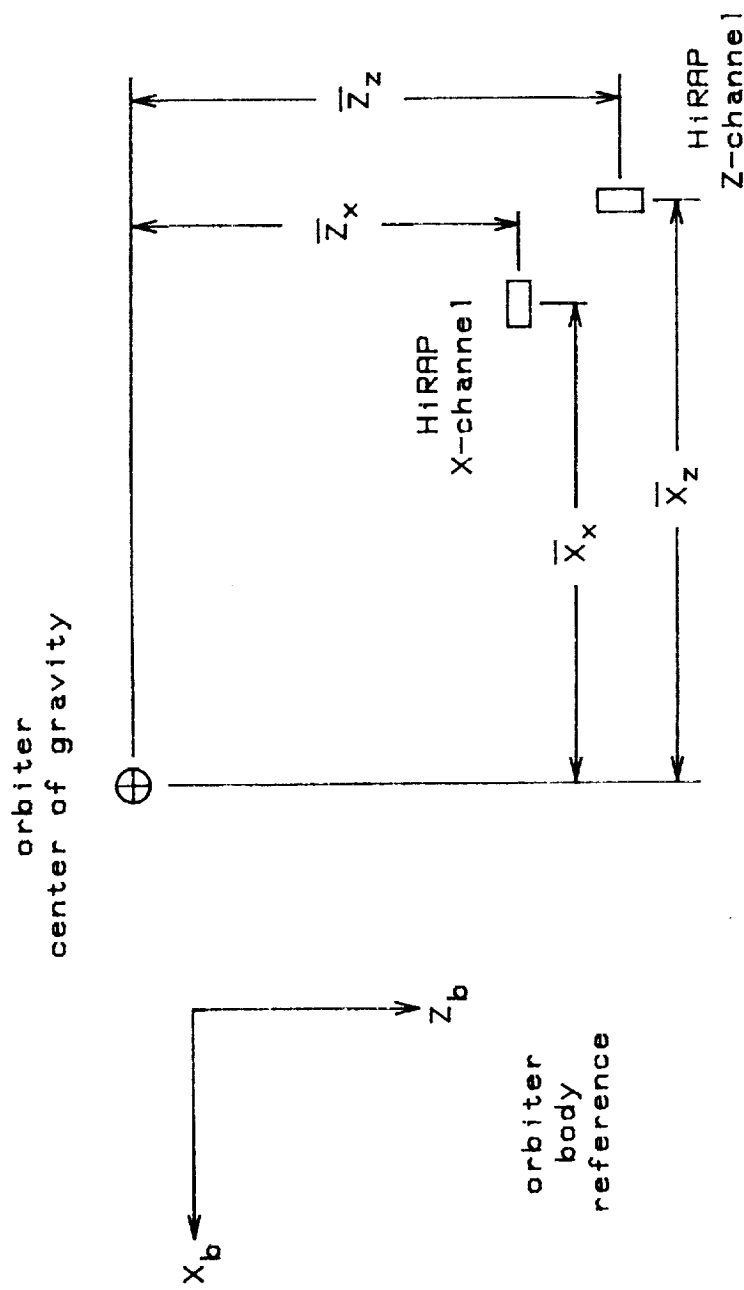
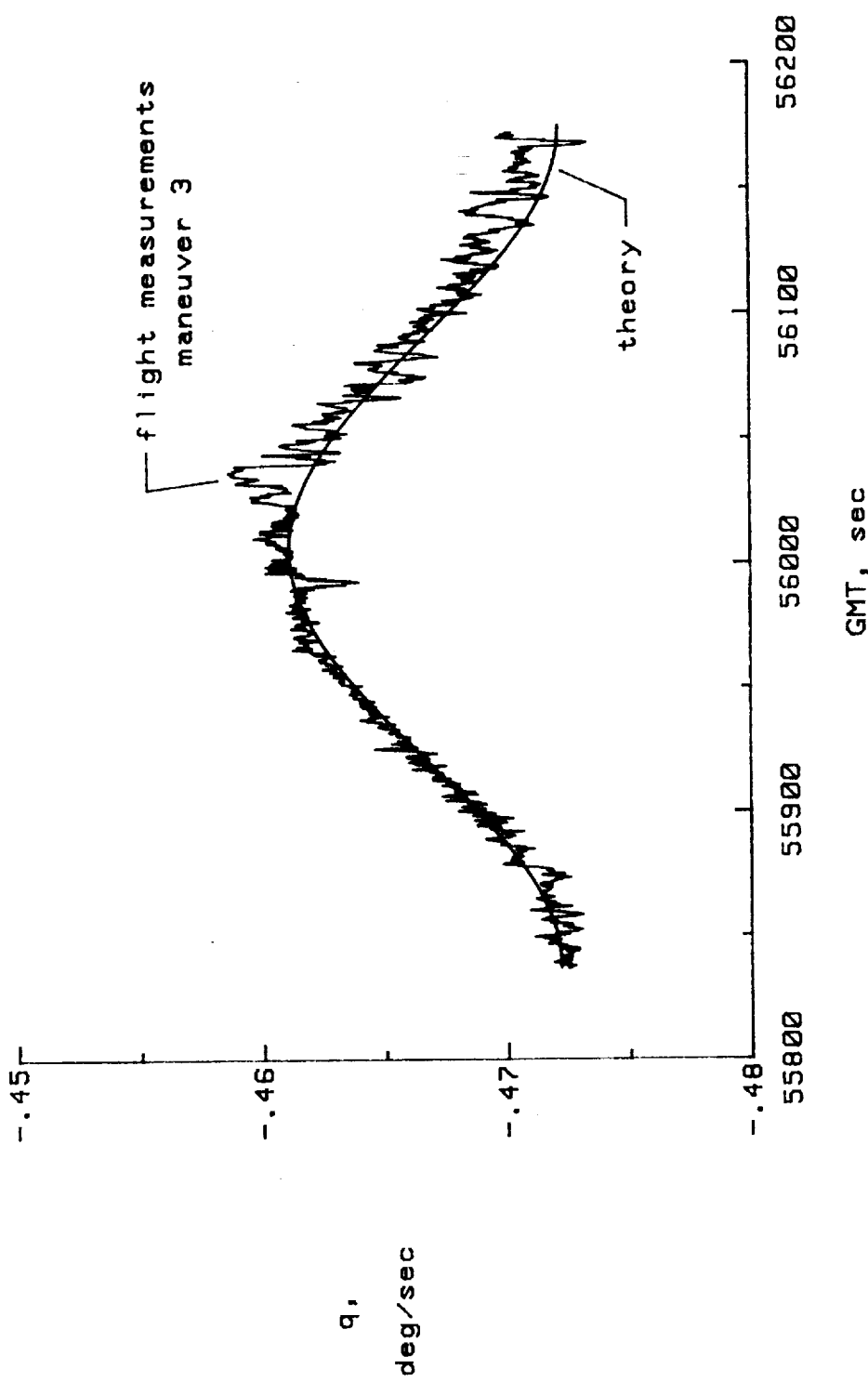


Figure 11. Convention for measurement of CG offsets.

Figure 12. Effect of gravity-gradient-induced acceleration on q .



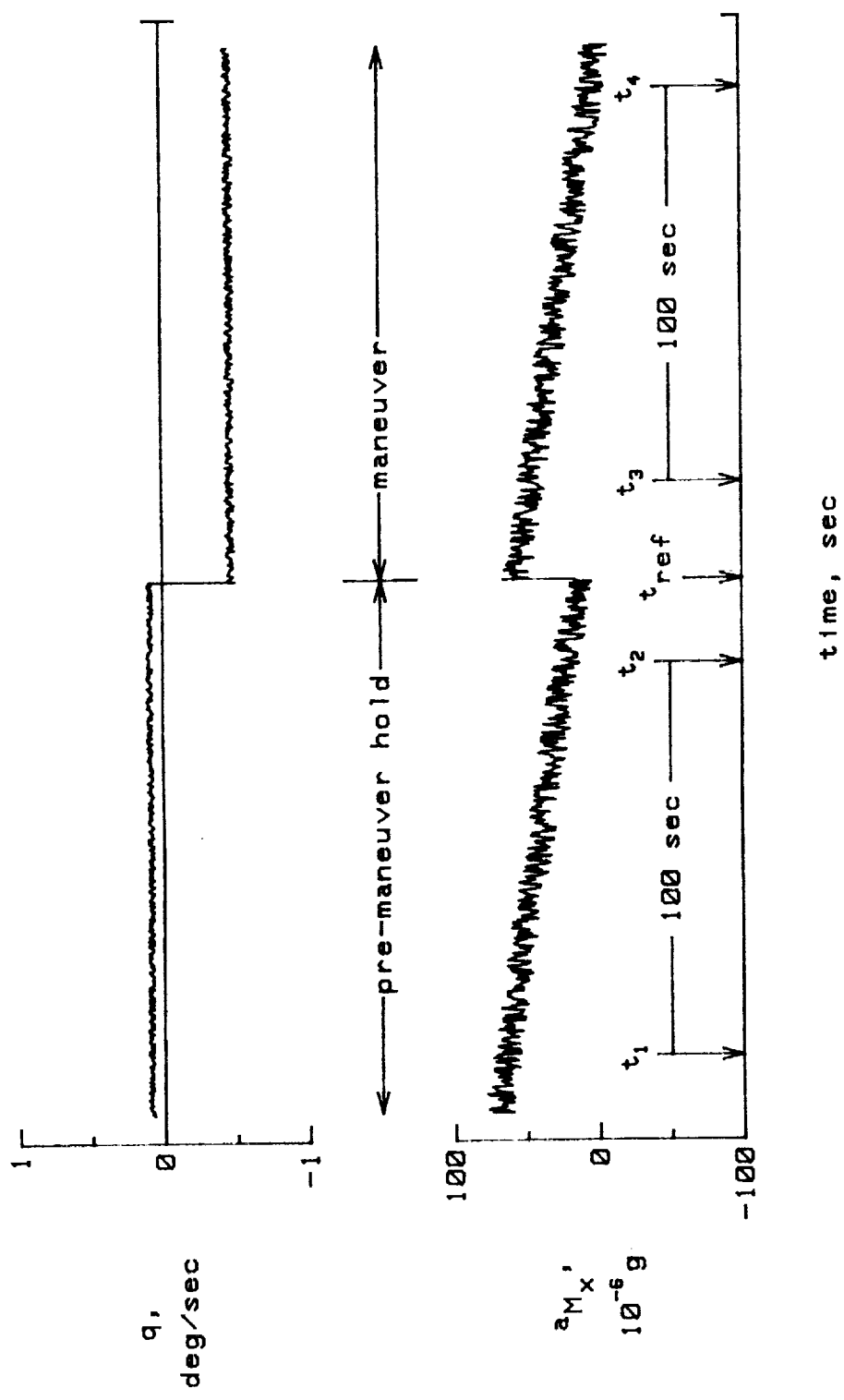


Figure 13. Description of data intervals for CG solution.

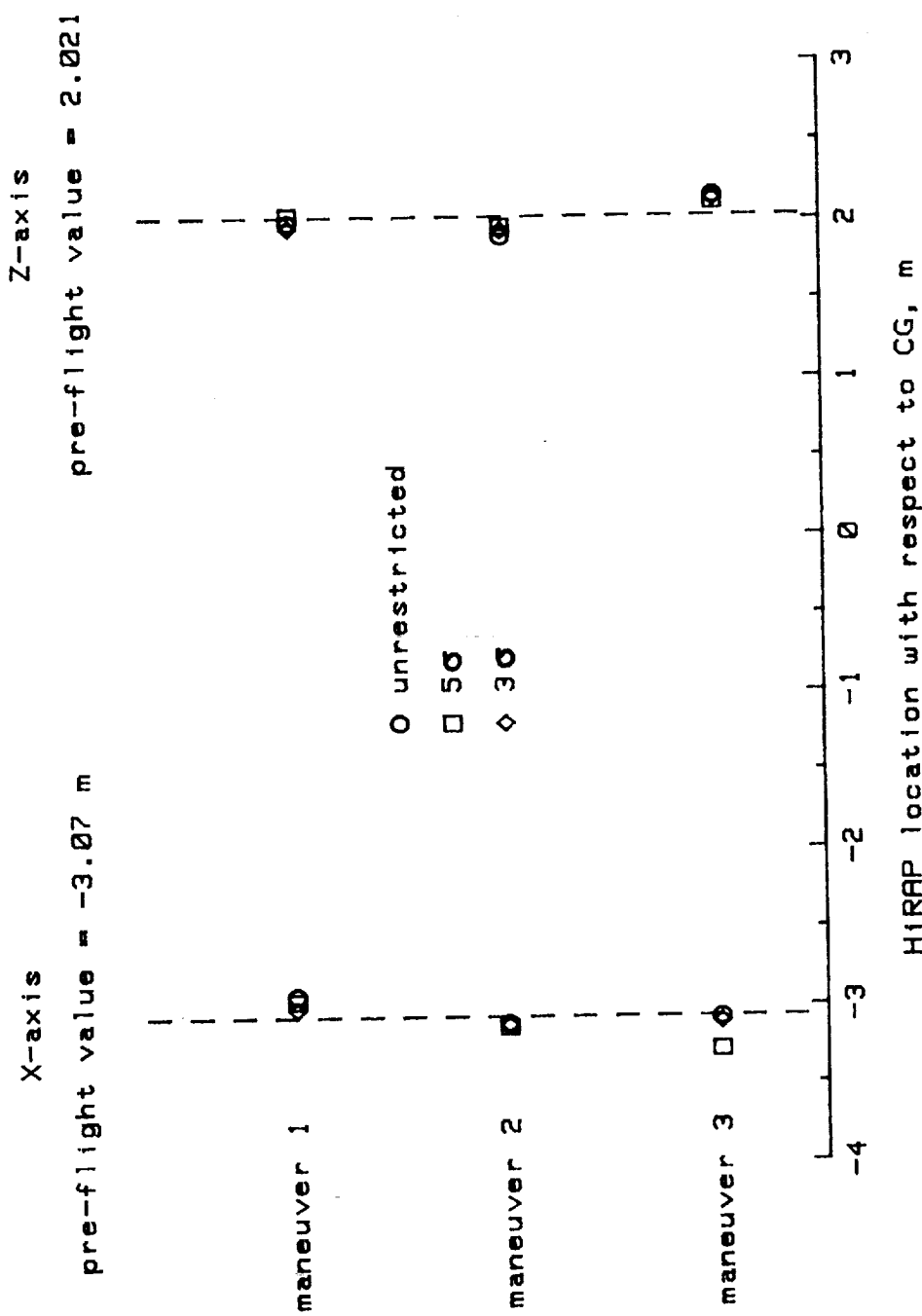
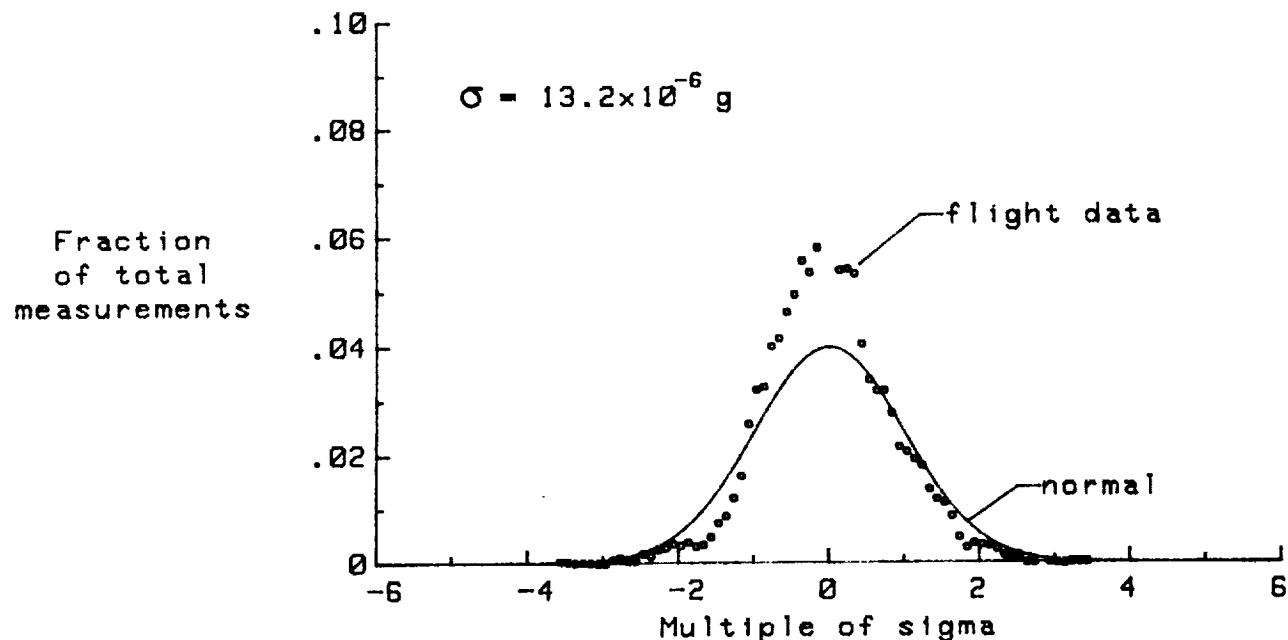
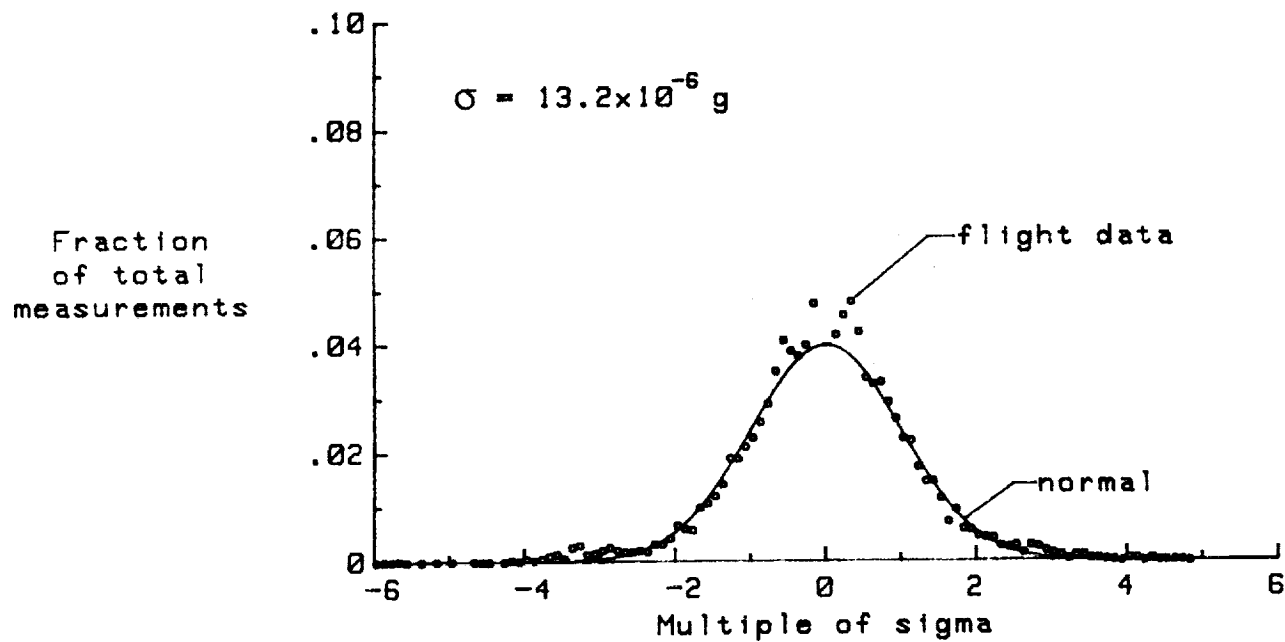


Figure 14. CG offsets determined from flight data.



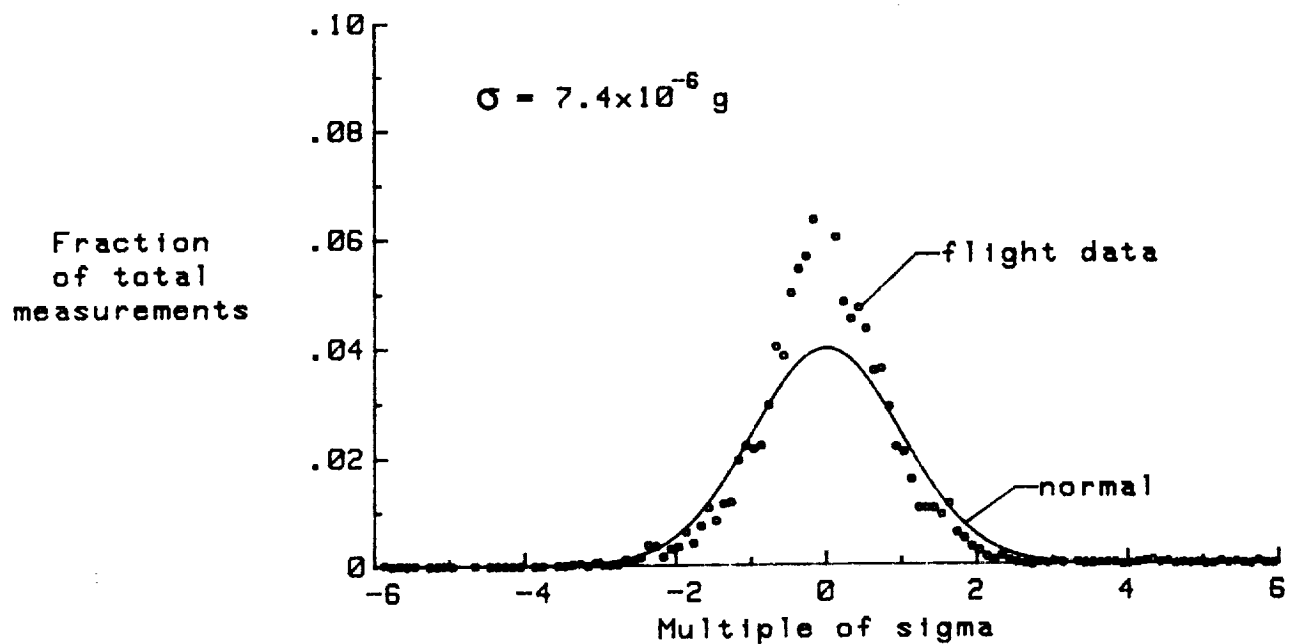
(a) Pre-maneuver segment

Figure 15. Distribution of residuals, maneuver 1,
X-axis unrestricted solution.



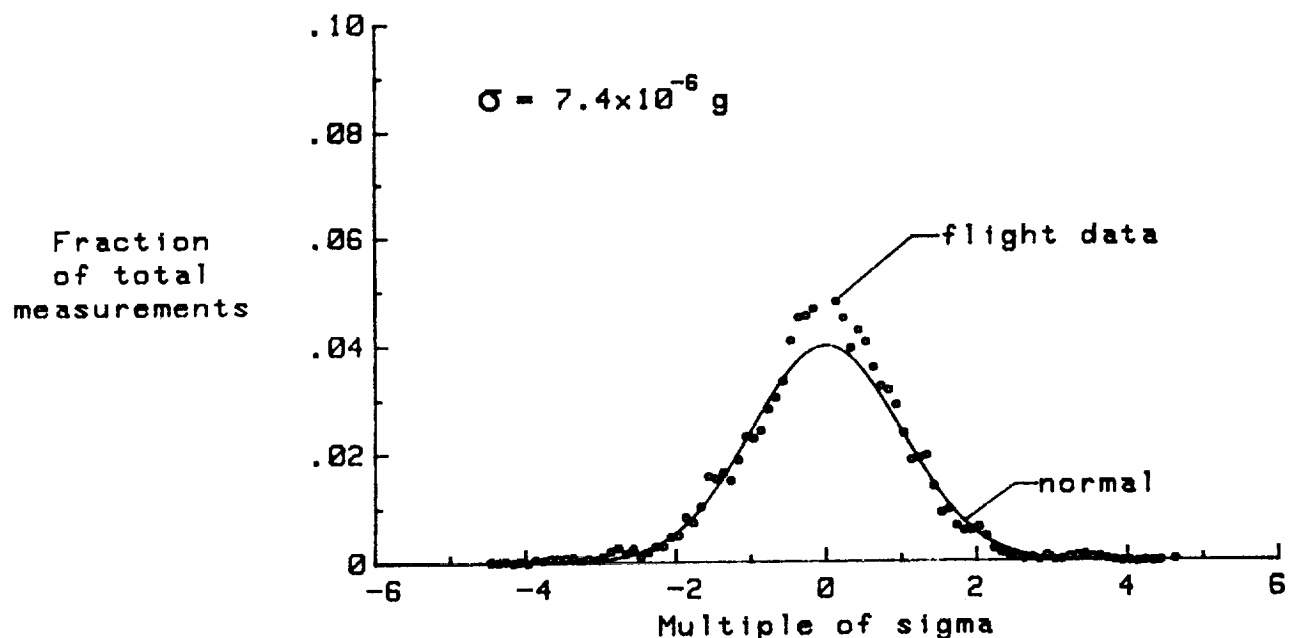
(b) Maneuver segment

Figure 15. Concluded.



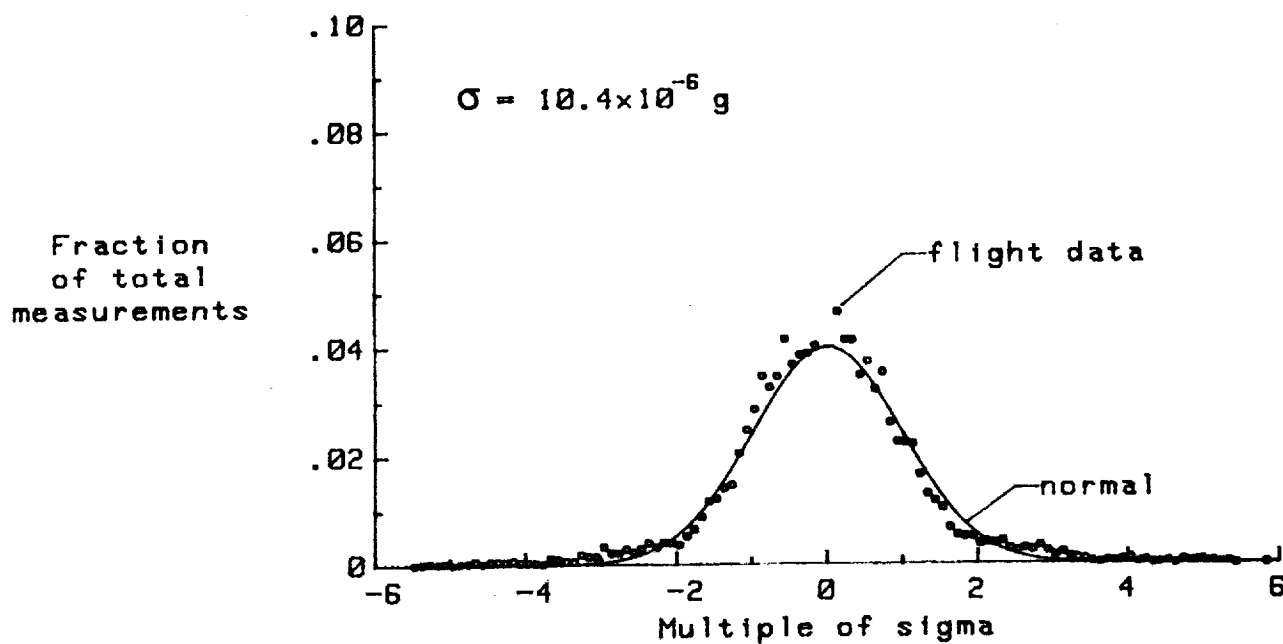
(a) Pre-maneuver segment

Figure 16. Distribution of residuals, maneuver 2,
X-axis unrestricted solution.



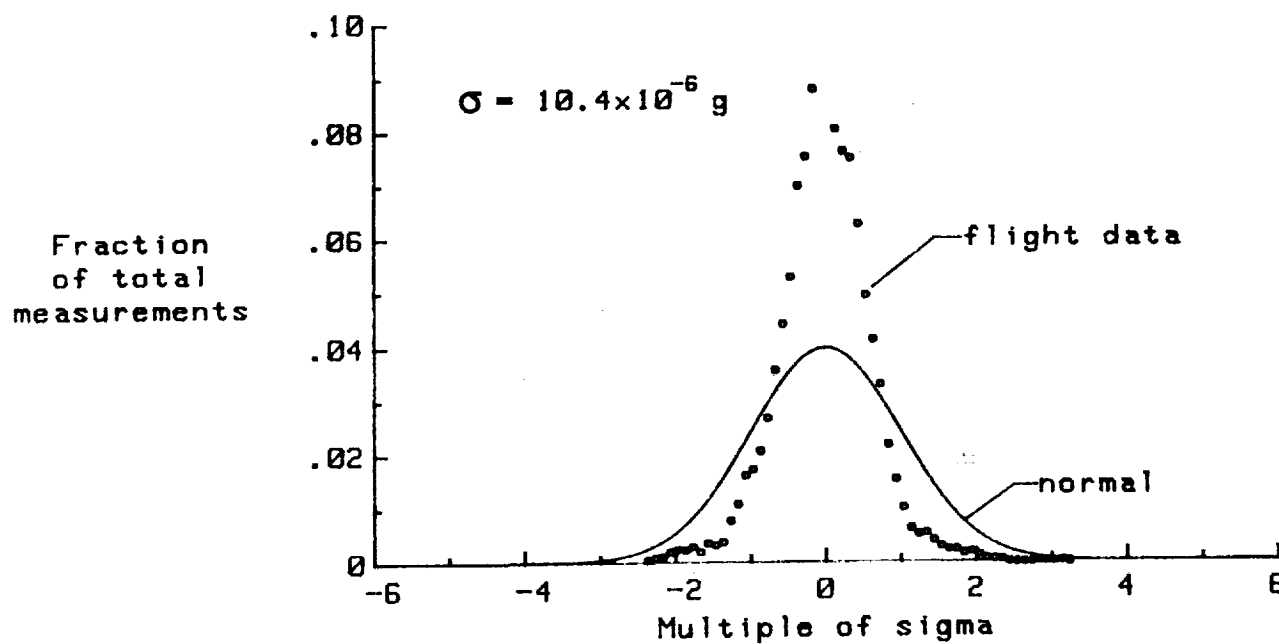
(b) Maneuver segment

Figure 16. Concluded.



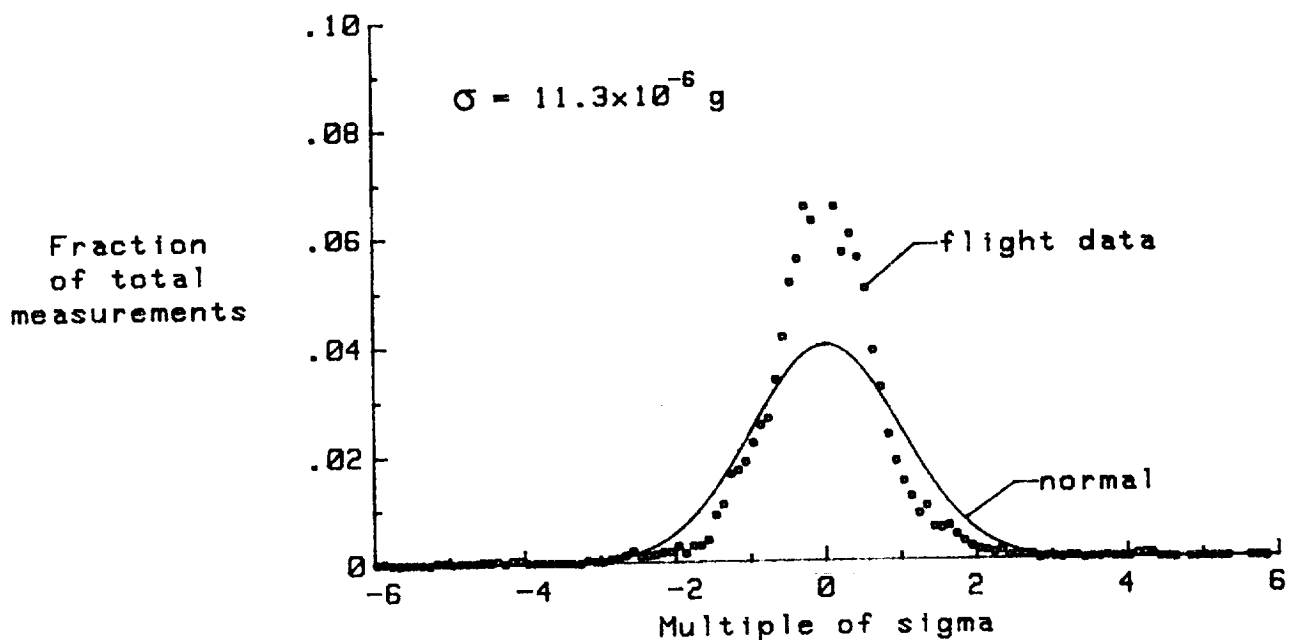
(a) Pre-maneuver segment

Figure 17. Distribution of residuals, maneuver 3,
X-axis unrestricted solution.



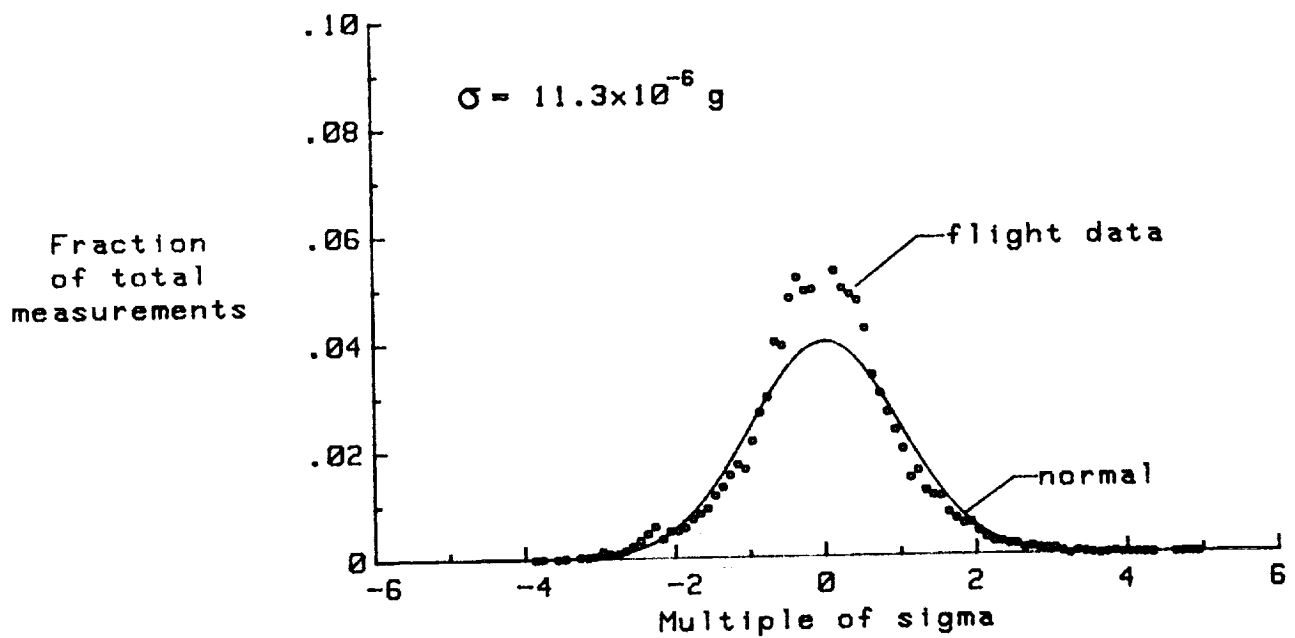
(b) Maneuver segment

Figure 17. Concluded.



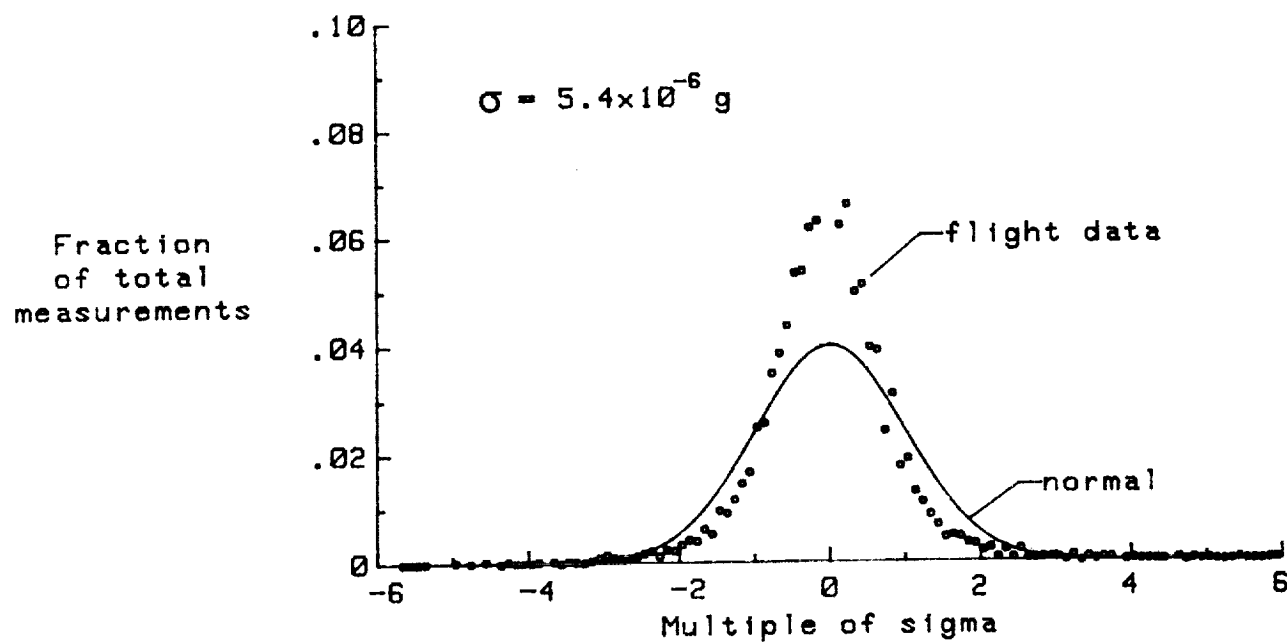
(a) Pre-maneuver segment

Figure 18. Distribution of residuals, maneuver 1,
Z-axis unrestricted solution.



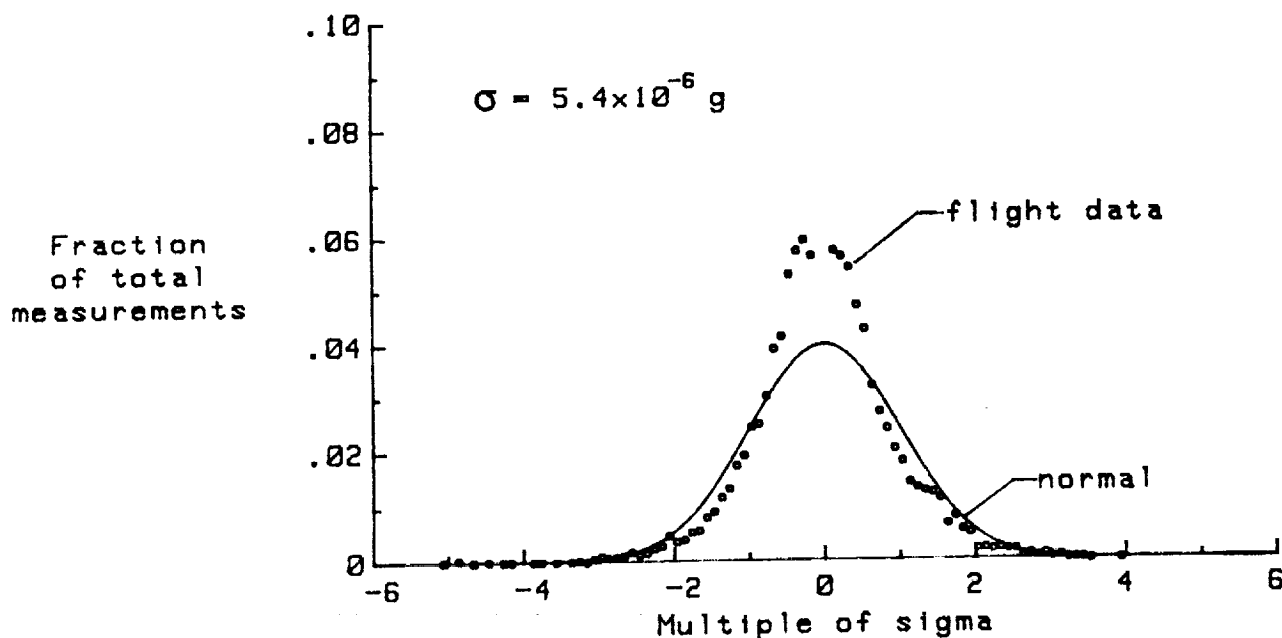
(b) Maneuver segment

Figure 18. Concluded.



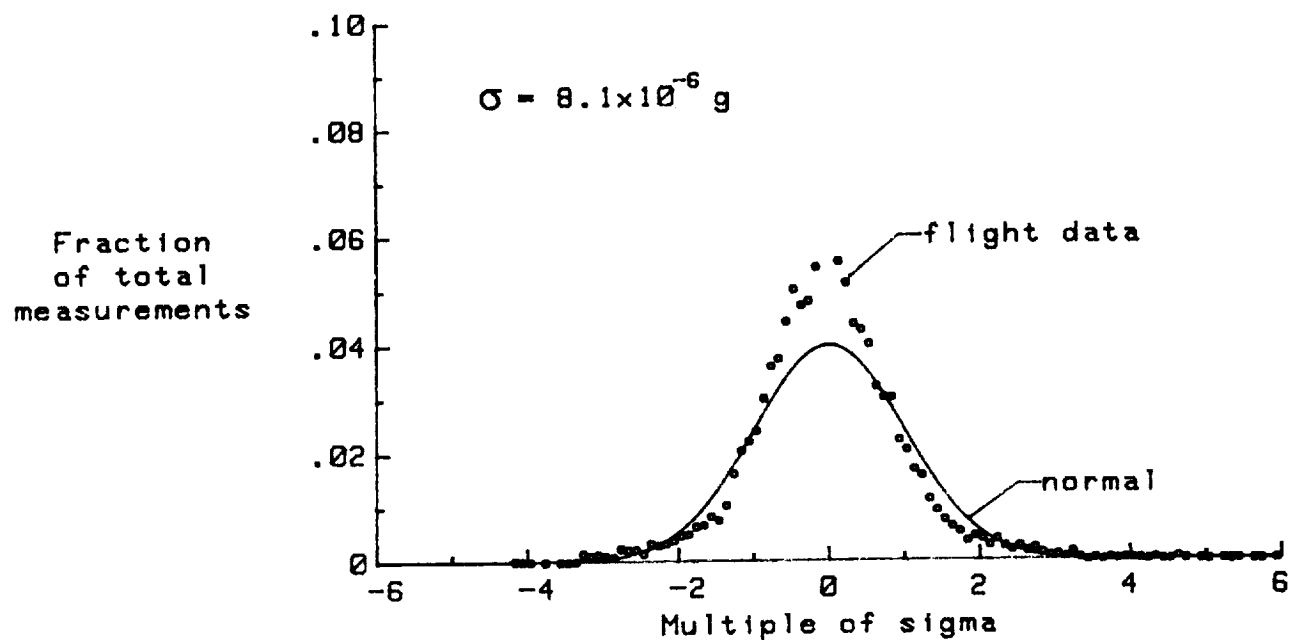
(a) Pre-maneuver segment

Figure 19. Distribution of residuals, maneuver 2,
Z-axis unrestricted solution.



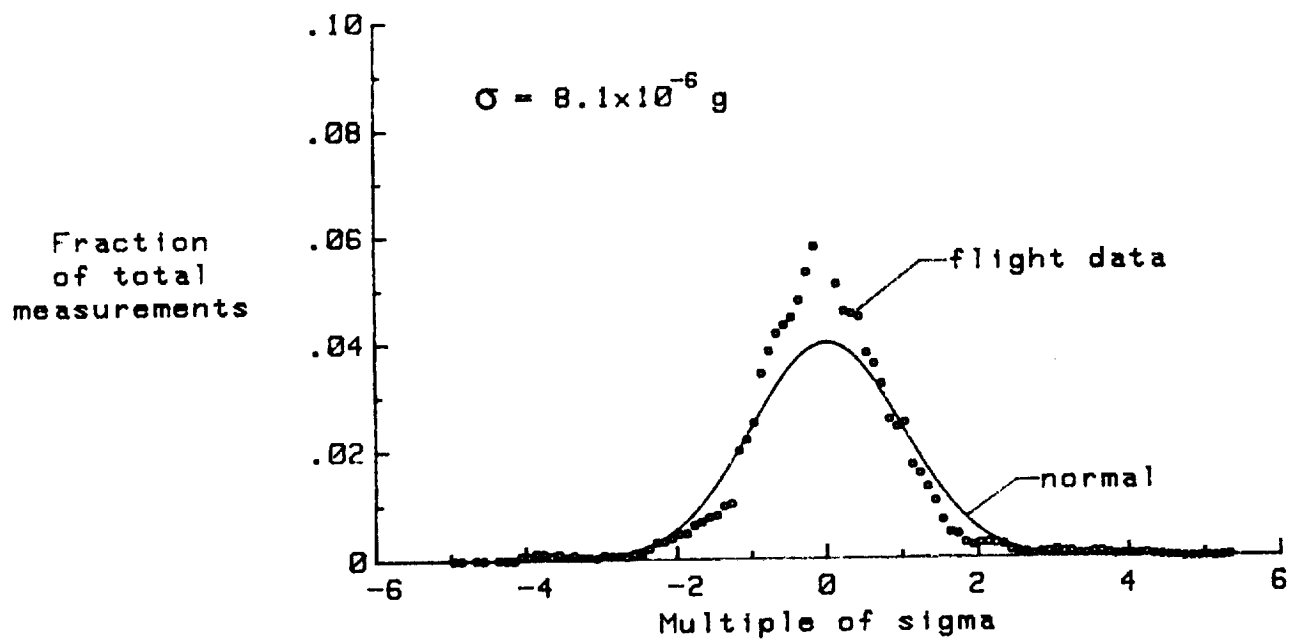
(b) Maneuver segment

Figure 19. Concluded.



(a) Pre-maneuver segment

Figure 20. Distribution of residuals, maneuver 3,
Z-axis unrestricted solution.



(b) Maneuver segment

Figure 20. Concluded.

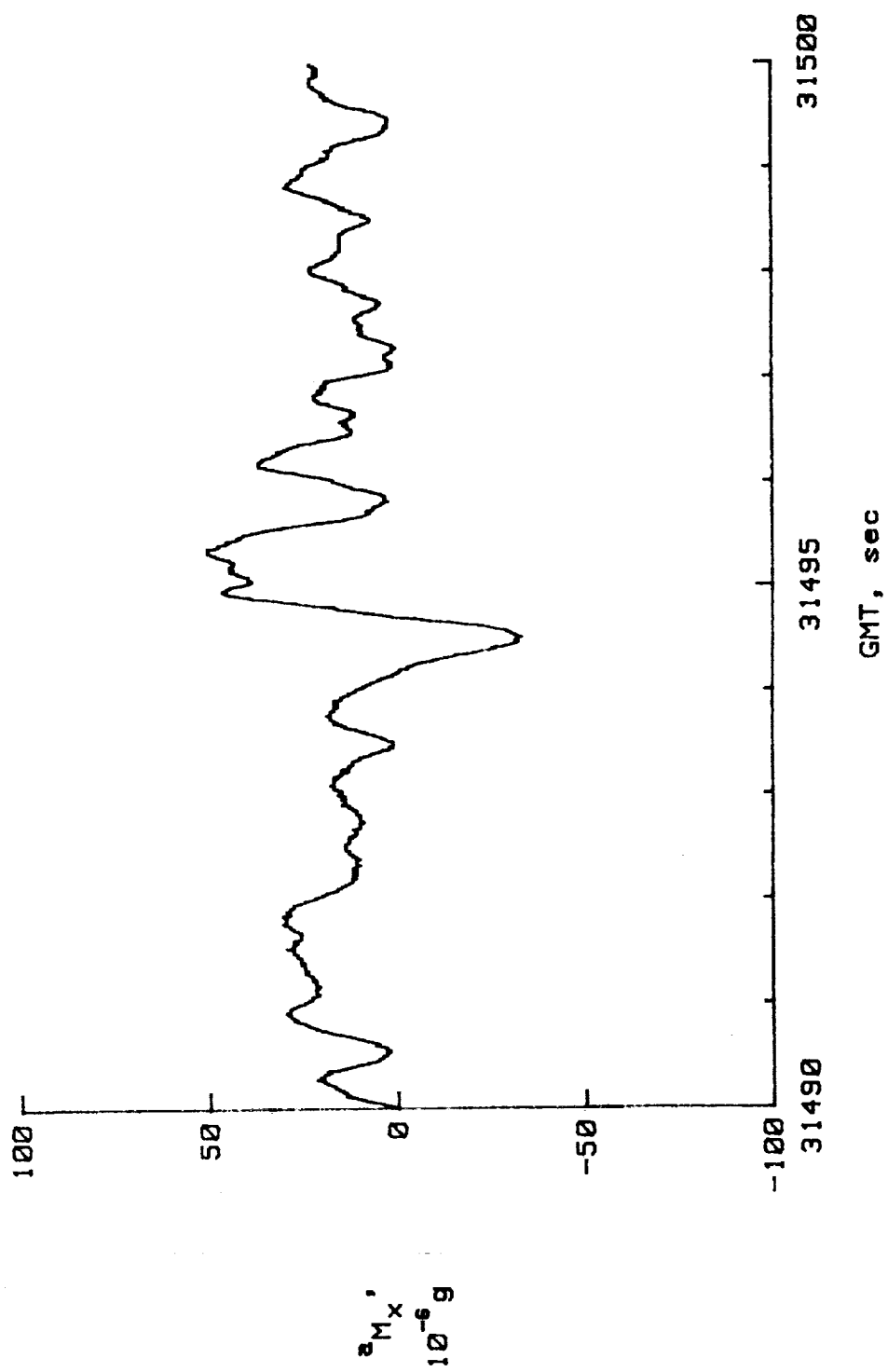
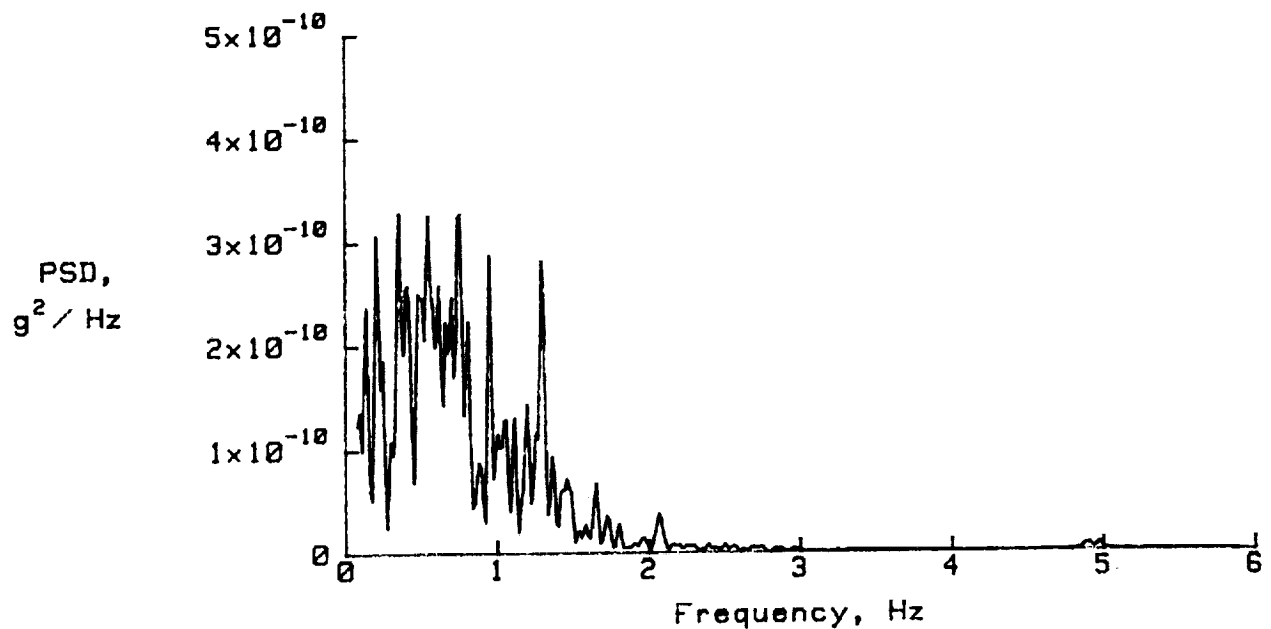
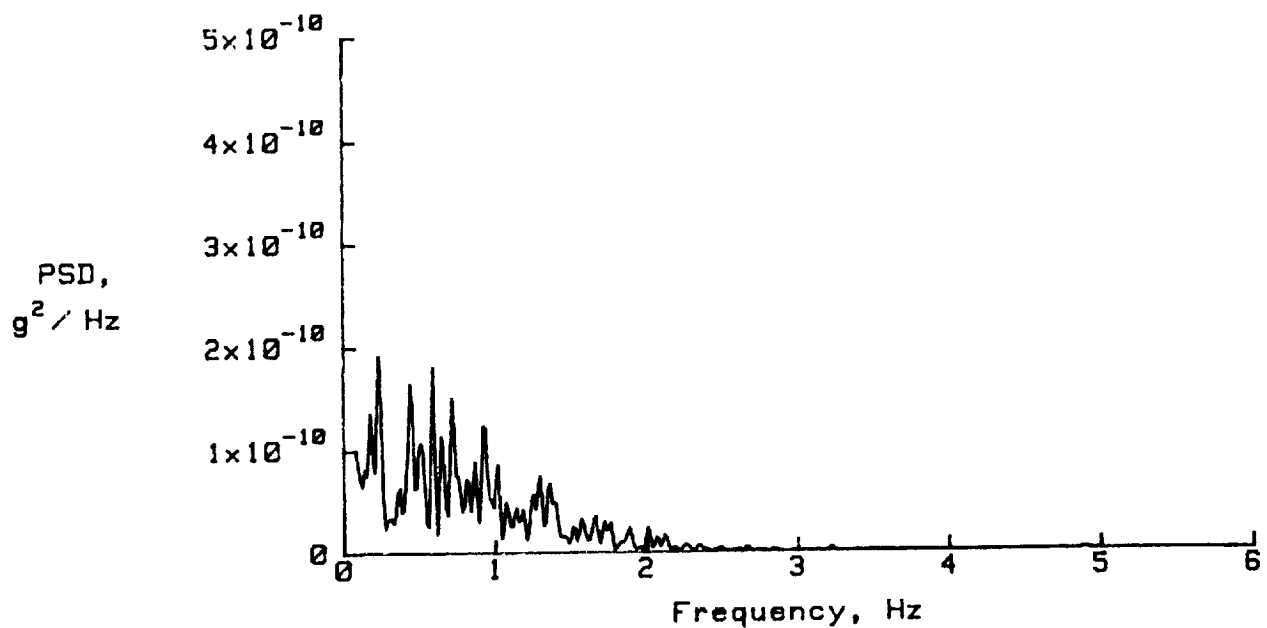


Figure 21. HIRAP X-channel relative output, maneuver 1, expanded scale.



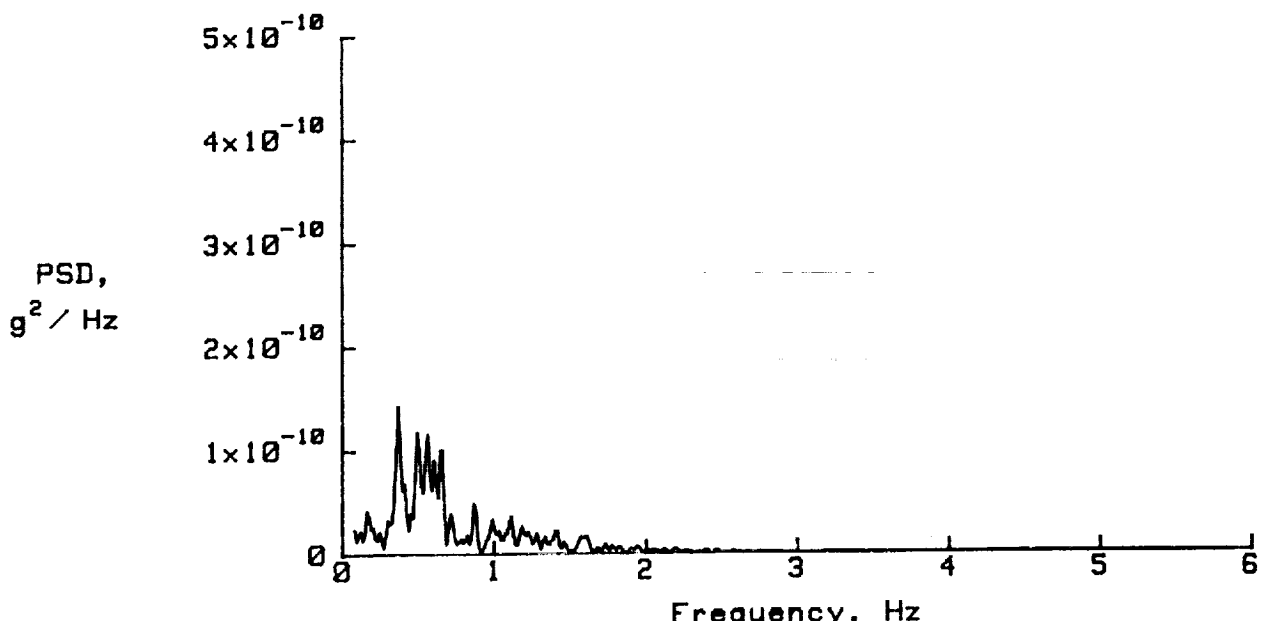
(a) Pre-maneuver segment

Figure 22. Power spectral density, maneuver 1, X-axis.



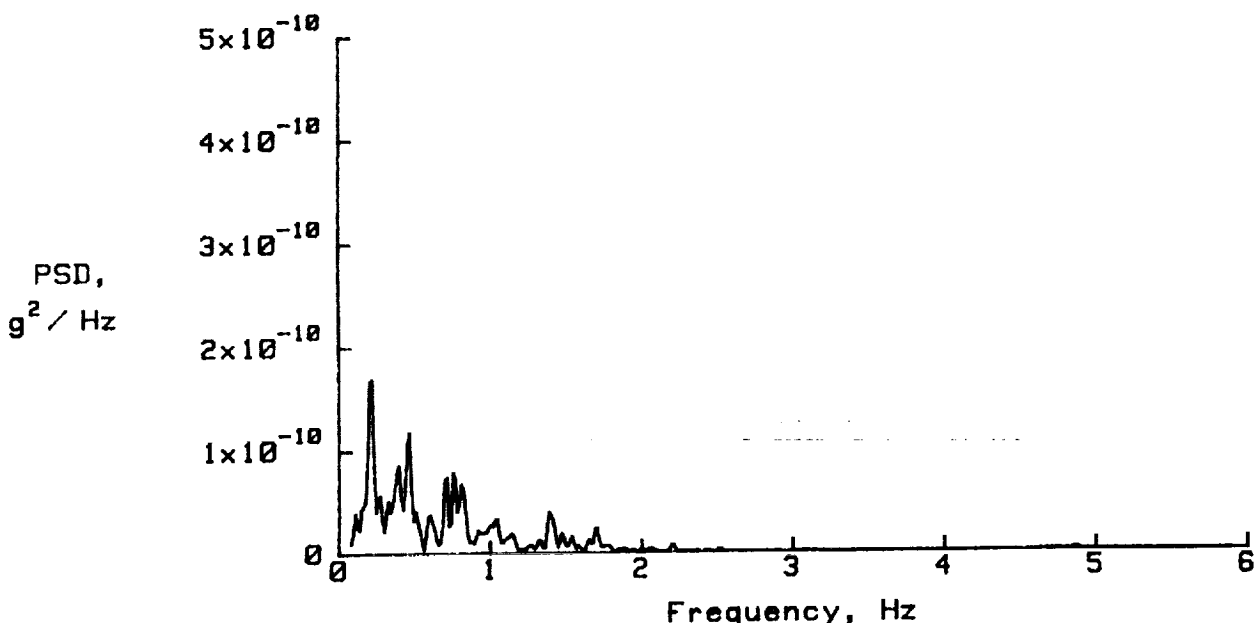
(b) Maneuver segment

Figure 22. Concluded.



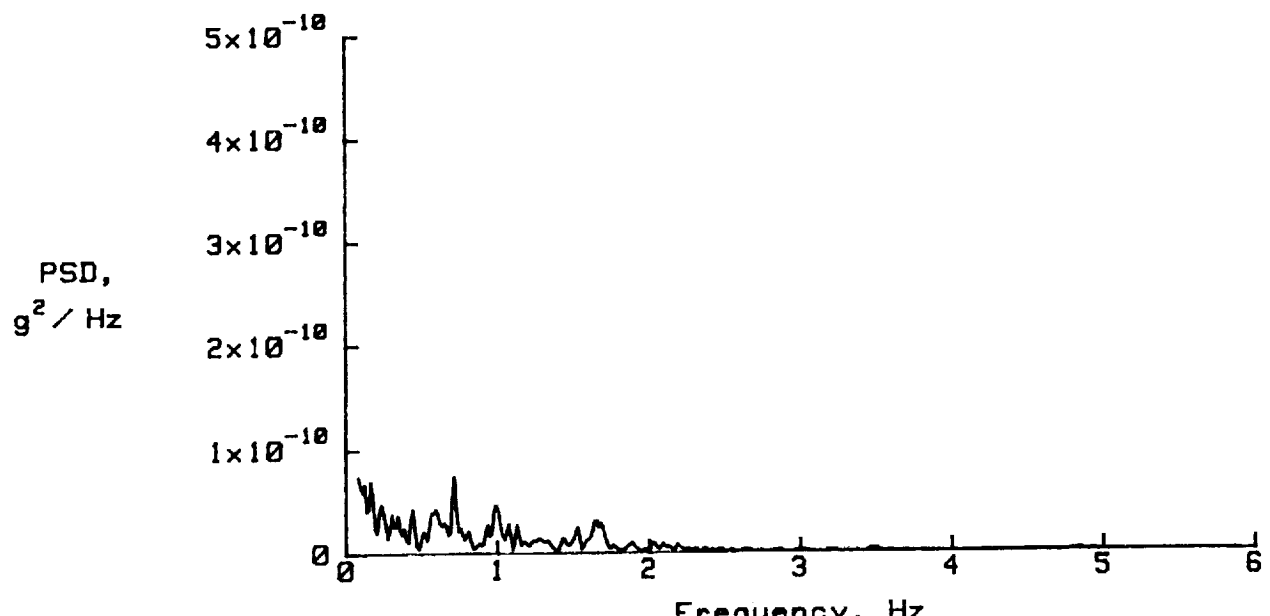
(a) Pre-manuever segment

Figure 23. Power spectral density, maneuver 2, X-axis.



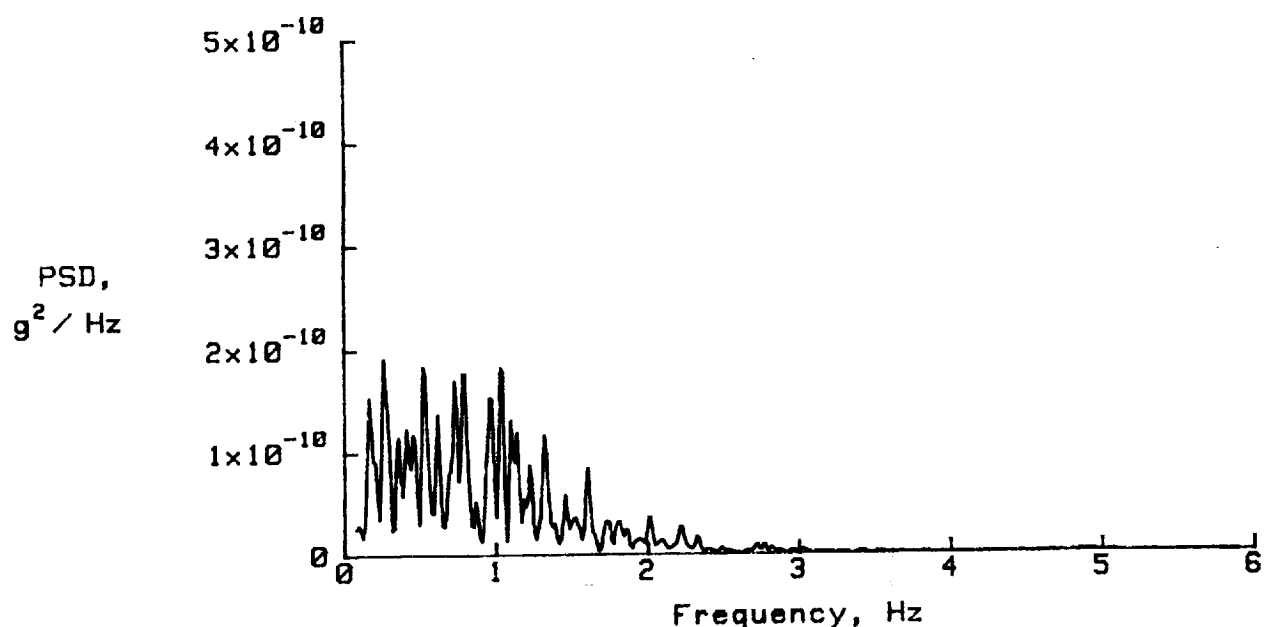
(b) Maneuver segment

Figure 23. Concluded.



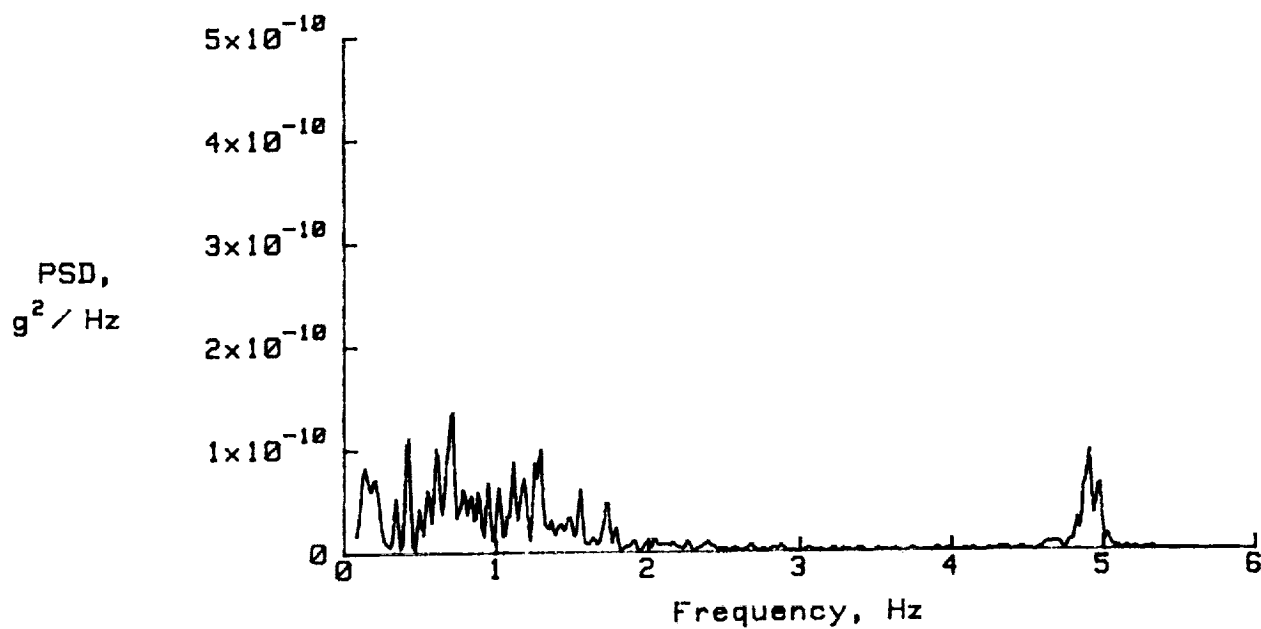
(a) Pre-manuever segment

Figure 24. Power spectral density, maneuver 3, X-axis.



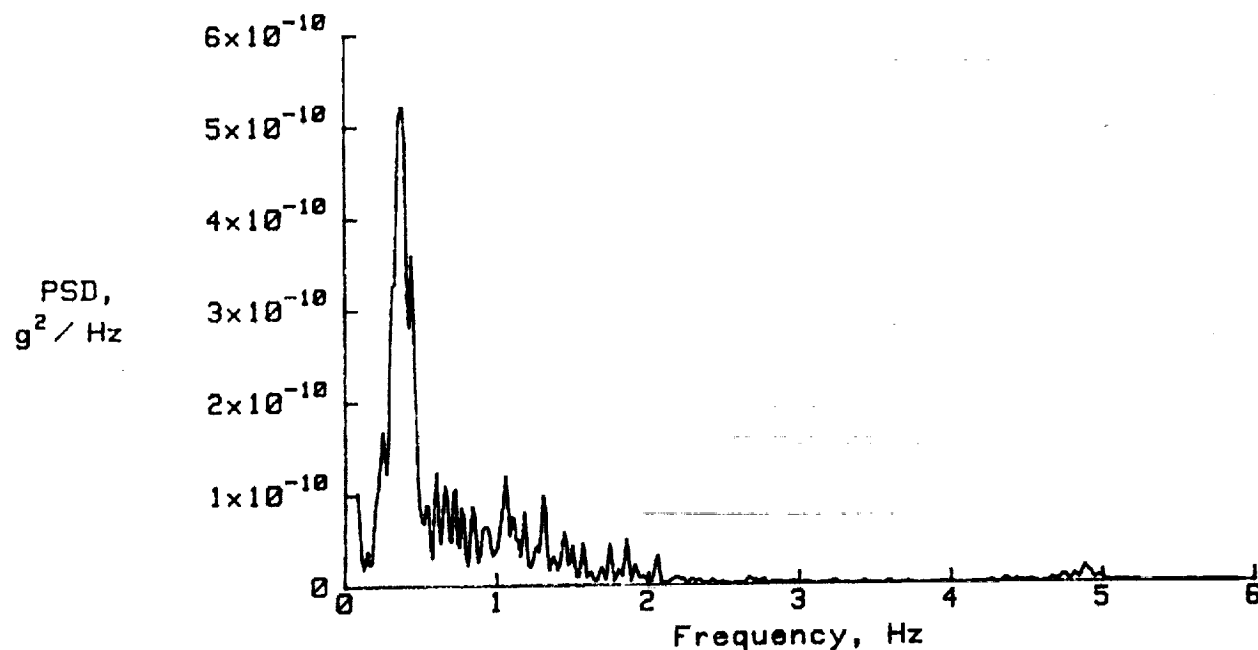
(b) Maneuver segment

Figure 24. Concluded.



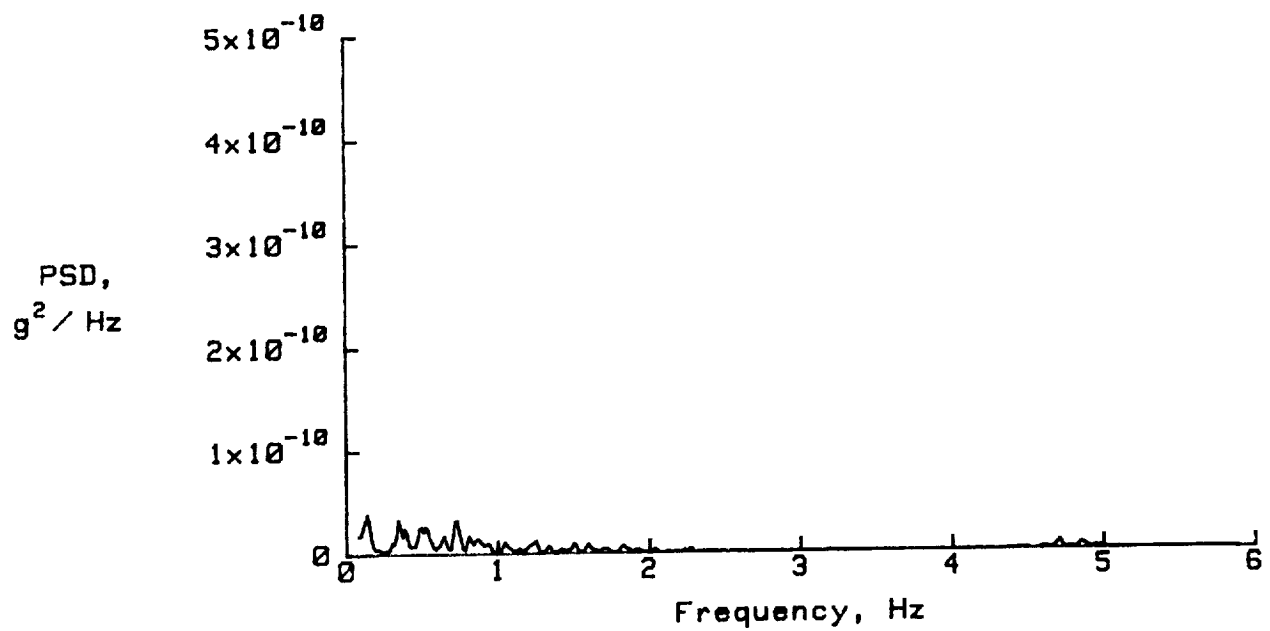
(a) Pre-maneuver segment

Figure 25. Power spectral density, maneuver 1, Z-axis.



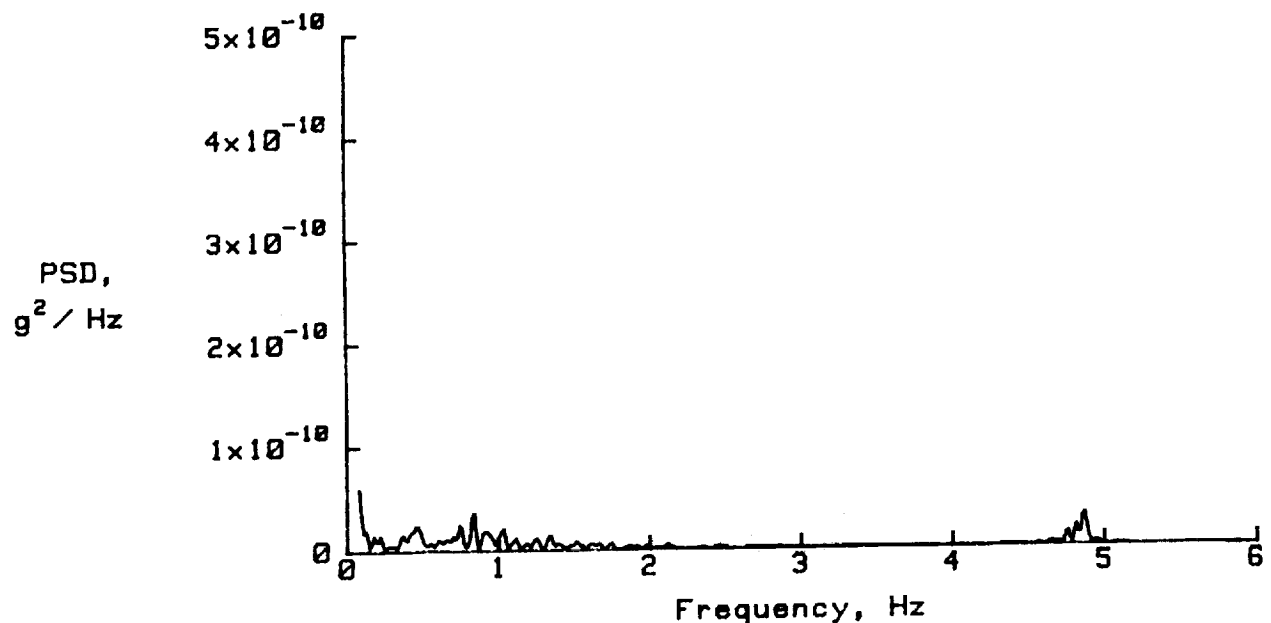
(b) Maneuver segment

Figure 25. Concluded.



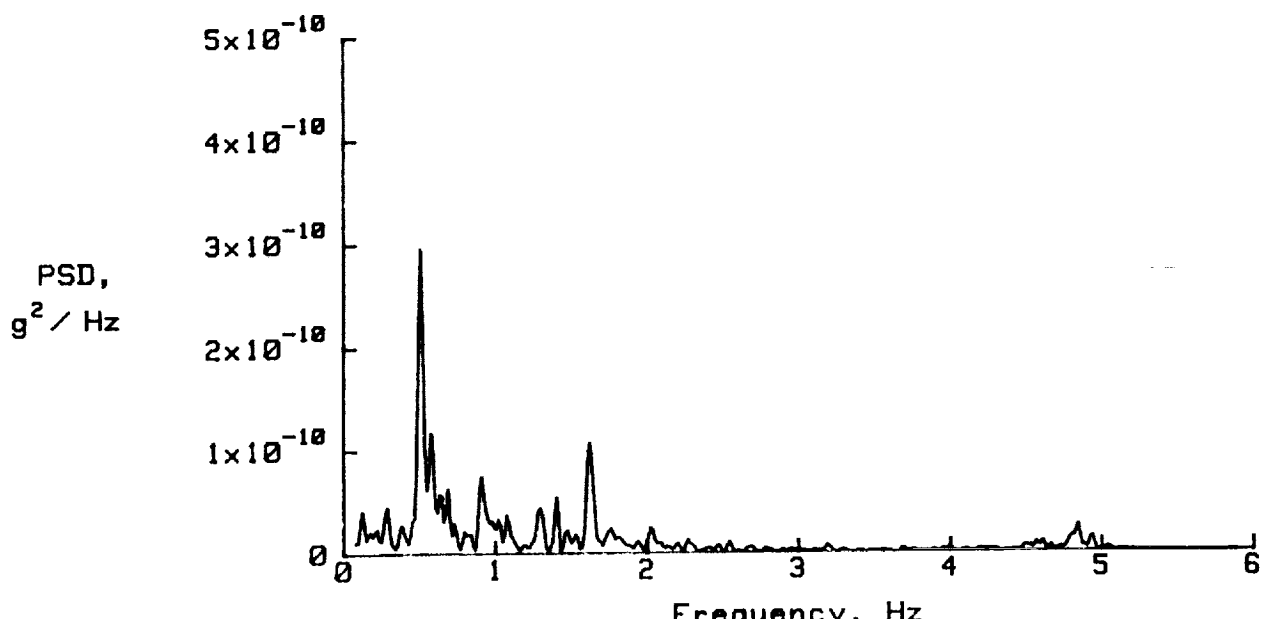
(a) Pre-manuever segment

Figure 26. Power spectral density, maneuver 2, Z-axis.



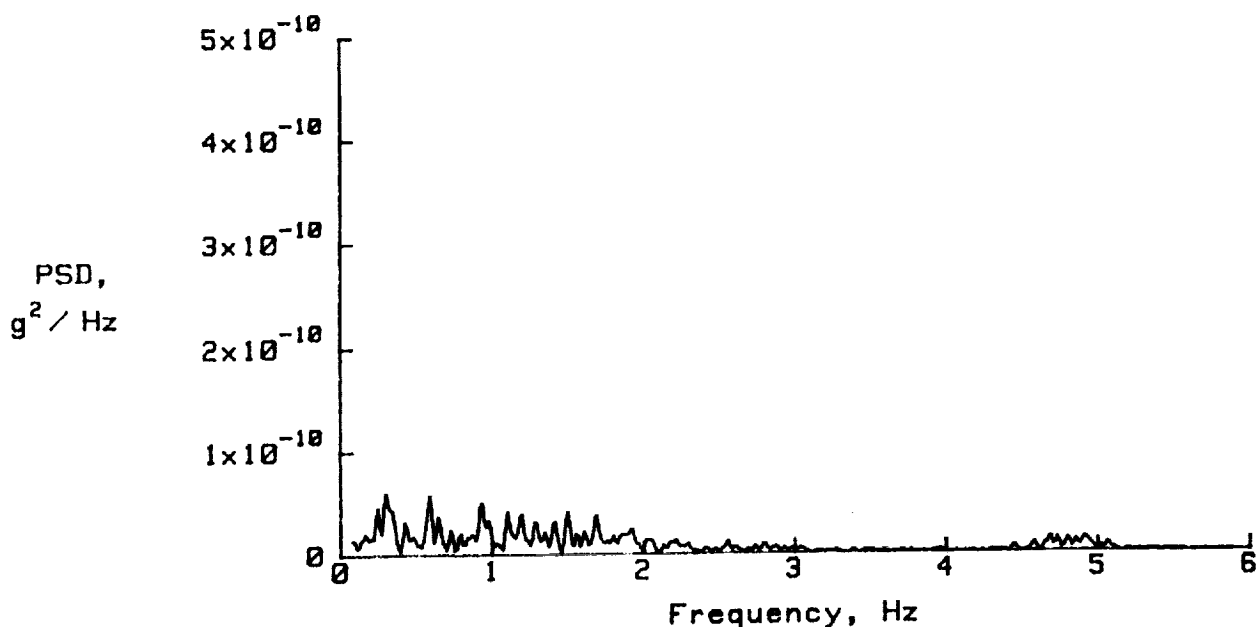
(b) Maneuver segment

Figure 26. Concluded.



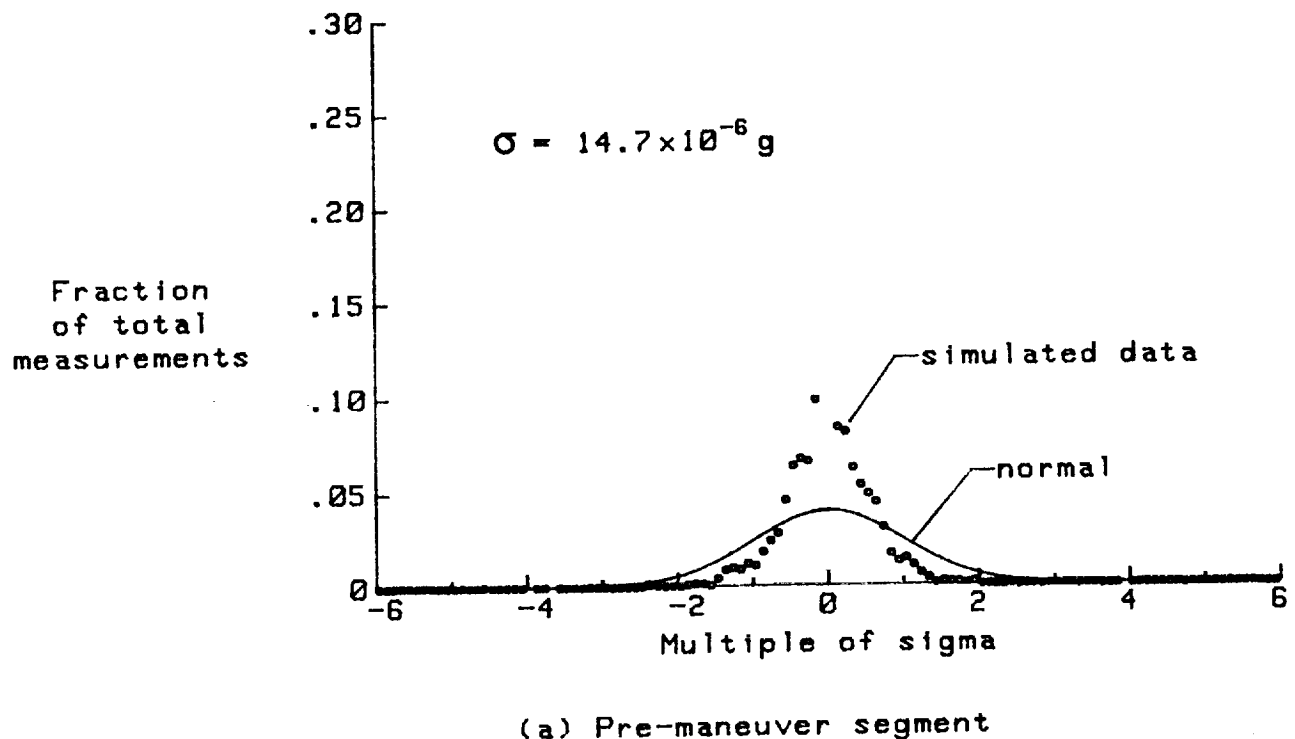
(a) Pre-manuever segment

Figure 27. Power spectral density, maneuver 3, Z-axis.



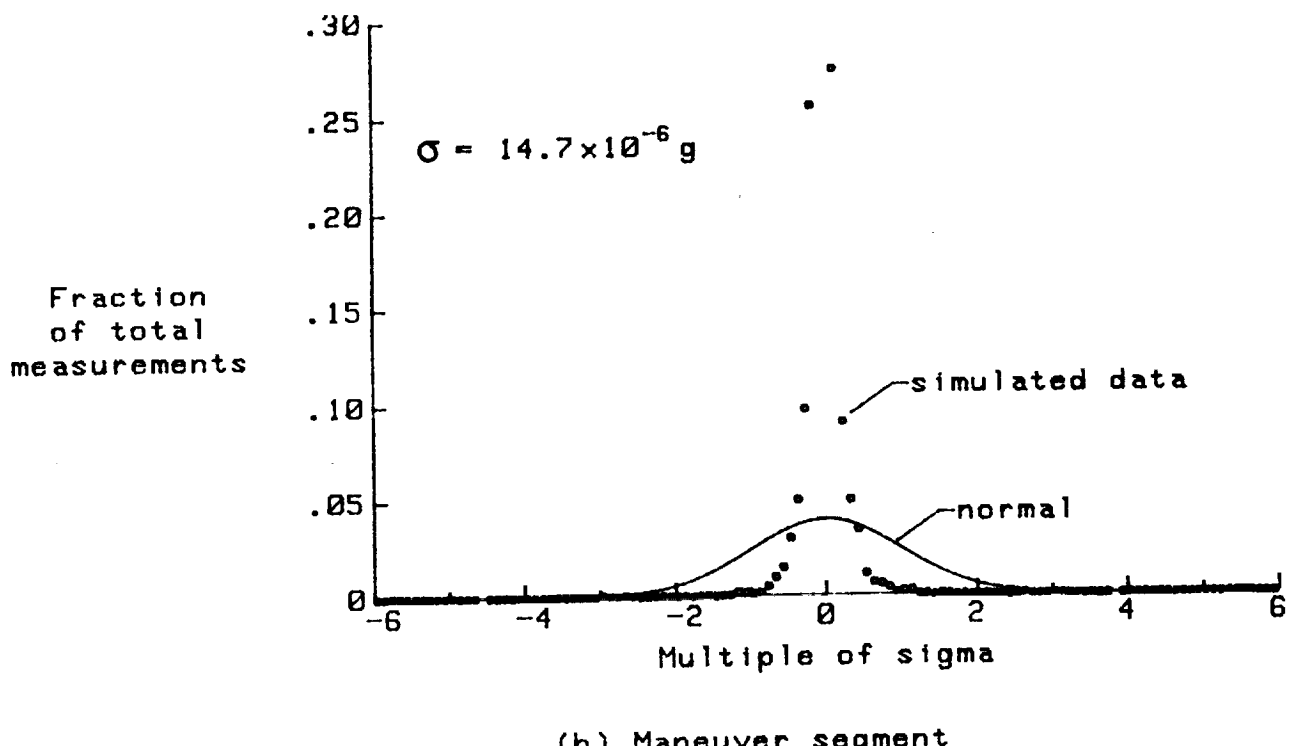
(b) Maneuver segment

Figure 27. Concluded.



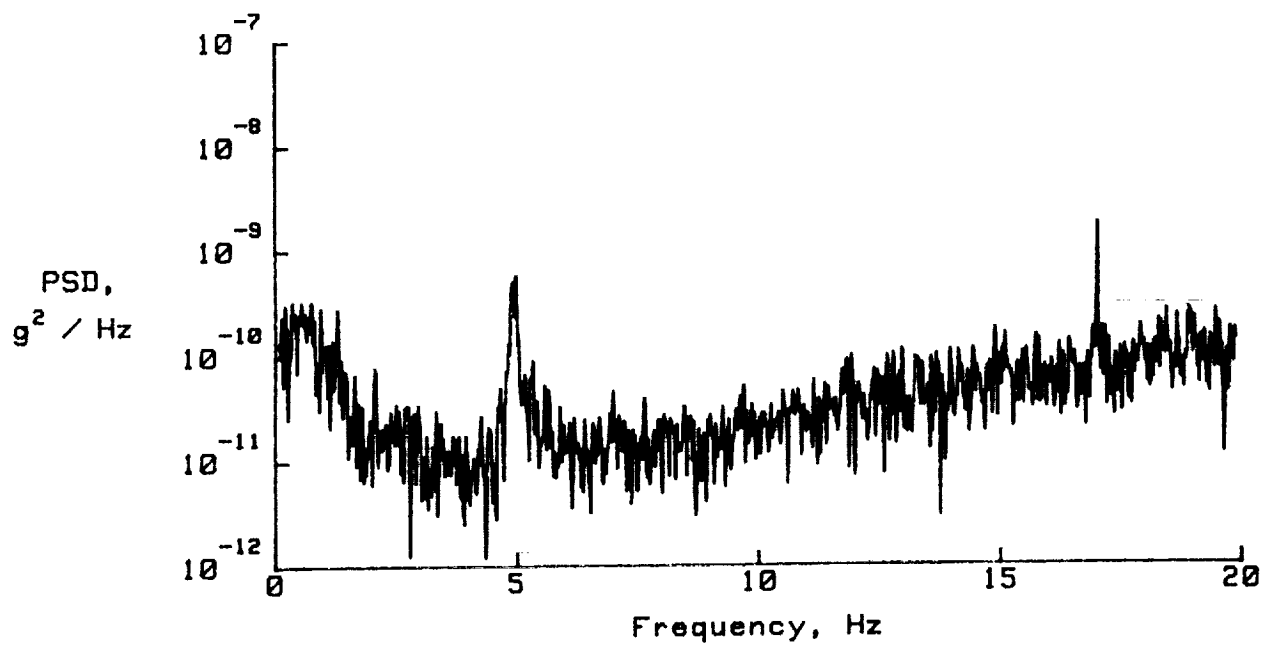
(a) Pre-maneuver segment

Figure 28. Distribution of residuals for simulated vibration.



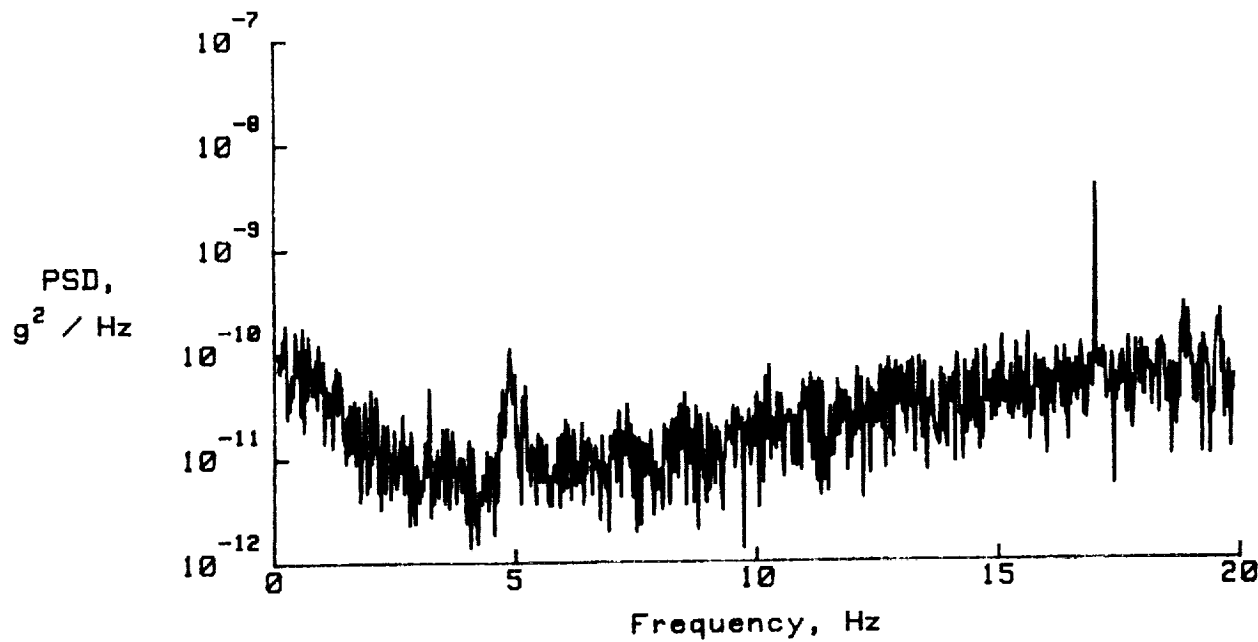
(b) Maneuver segment

Figure 28. Concluded.



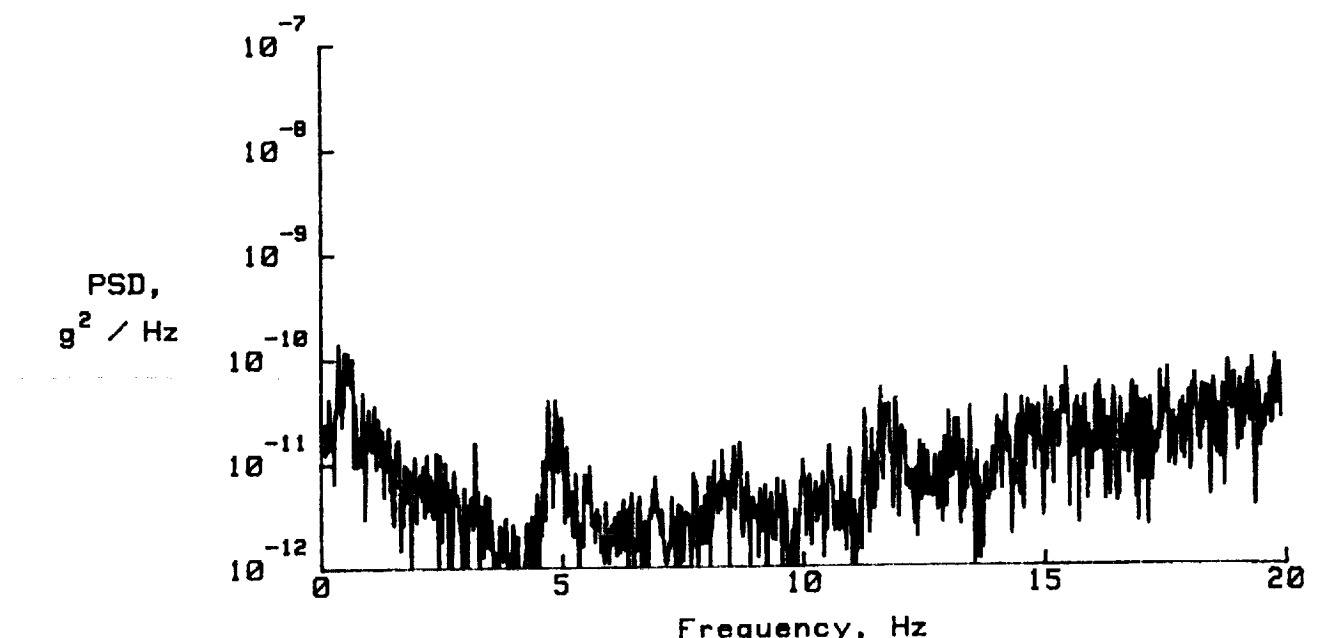
(a) Pre-maneuver segment

Figure 29. Unfiltered power spectral density, maneuver 1, X-axis.



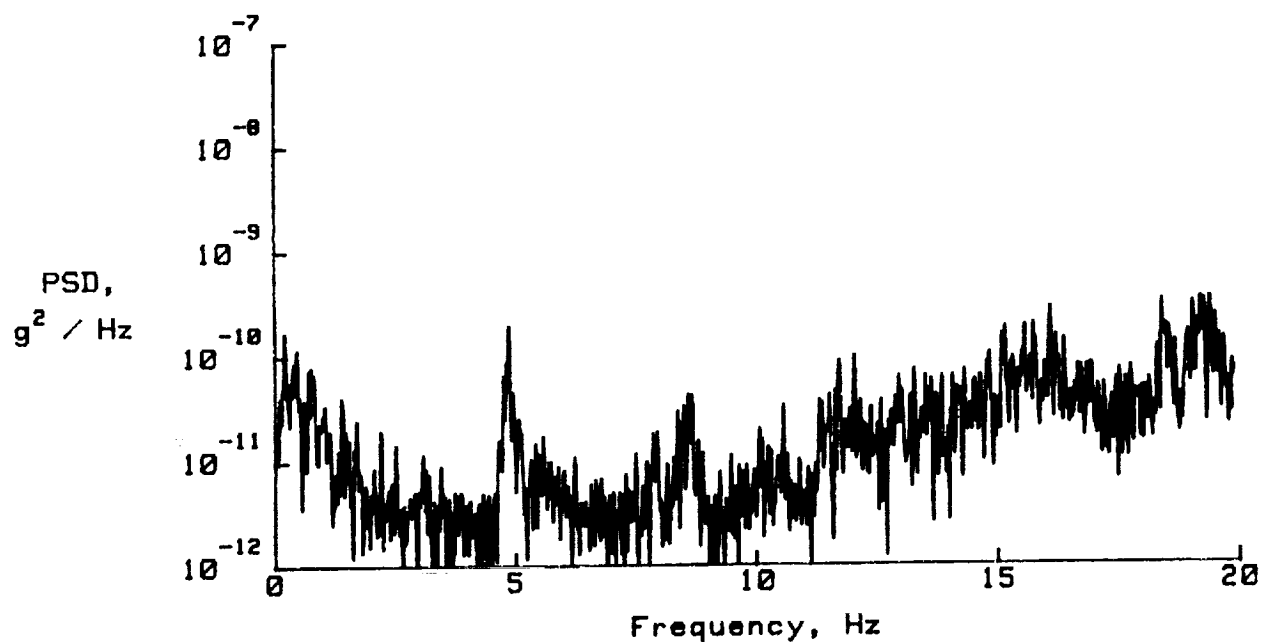
(b) Maneuver segment

Figure 29. Concluded.



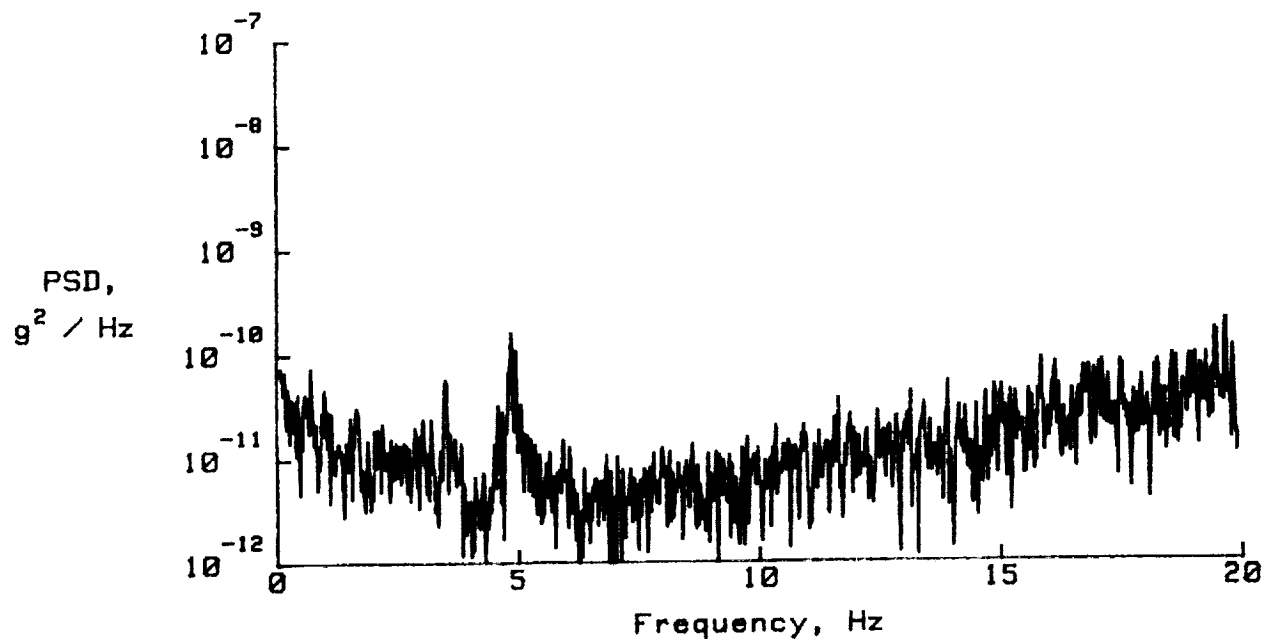
(a) Pre-maneuver segment

Figure 30. Unfiltered power spectral density, maneuver 2, X-axis.



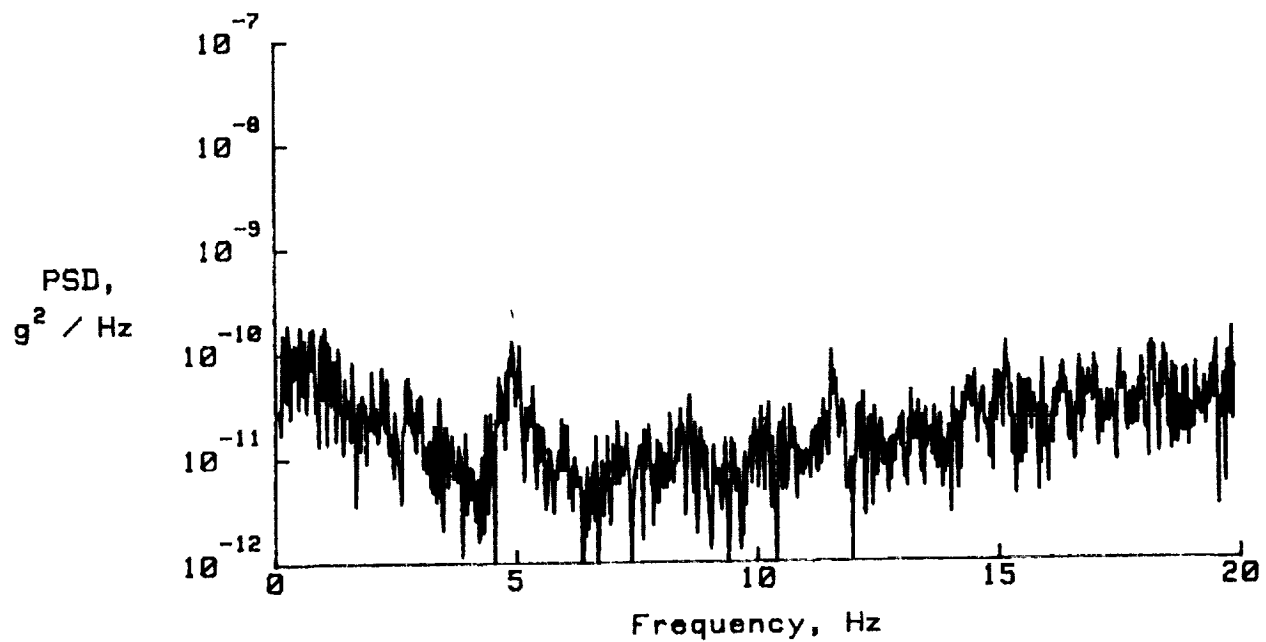
(b) Maneuver segment

Figure 30. Concluded.



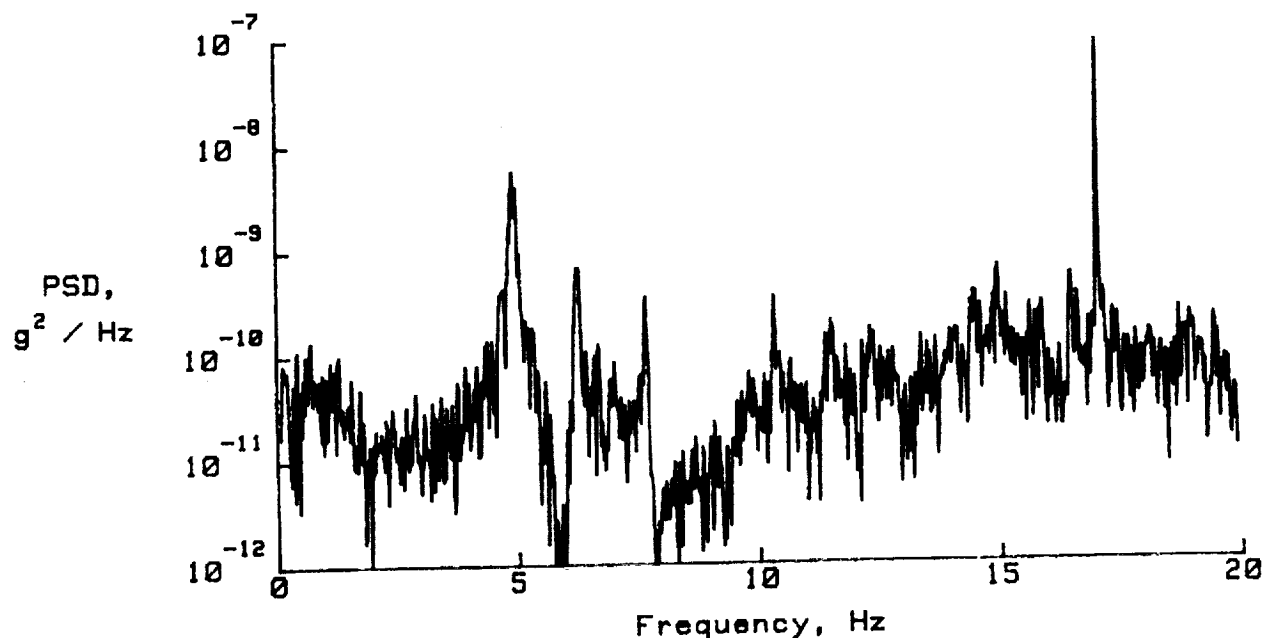
(a) Pre-maneuver segment

Figure 31. Unfiltered power spectral density, maneuver 3, X-axis.



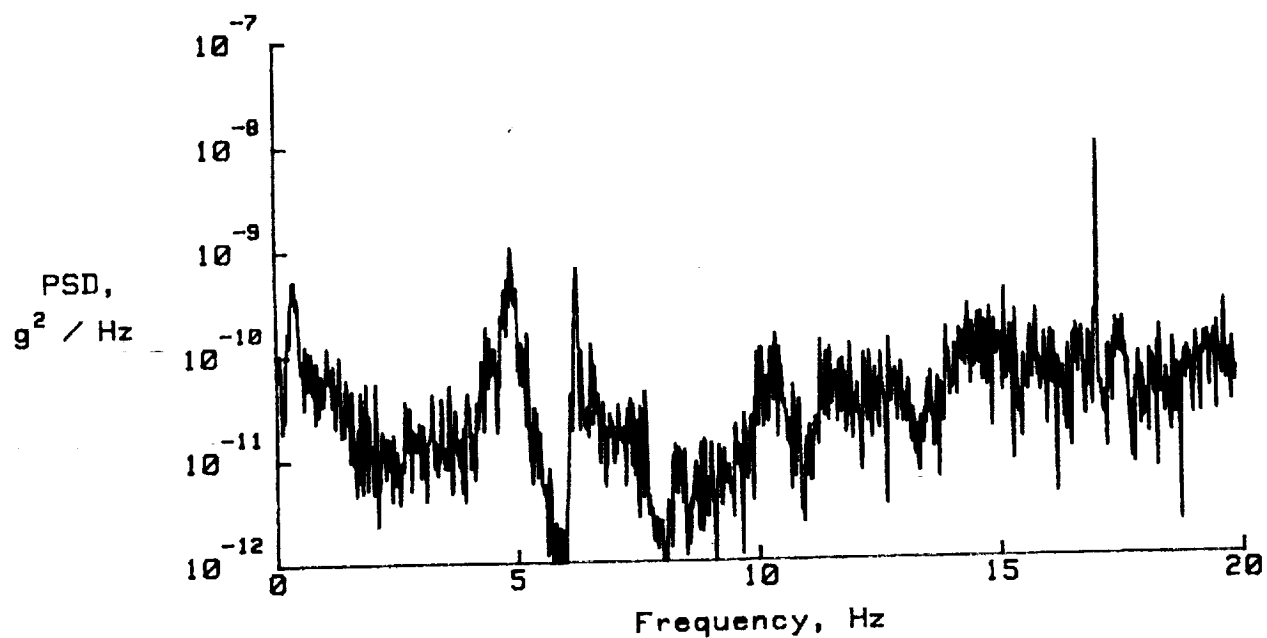
(b) Maneuver segment

Figure 31. Concluded.



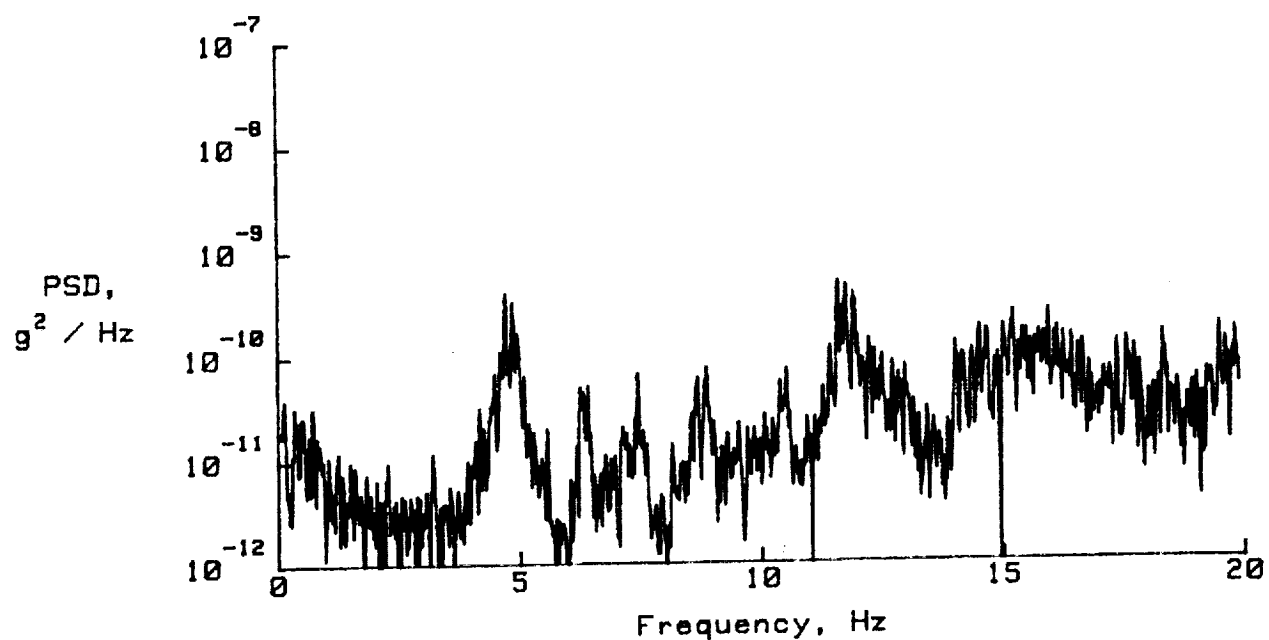
(a) Pre-maneuver segment

Figure 32. Unfiltered power spectral density, maneuver 1, Z-axis.



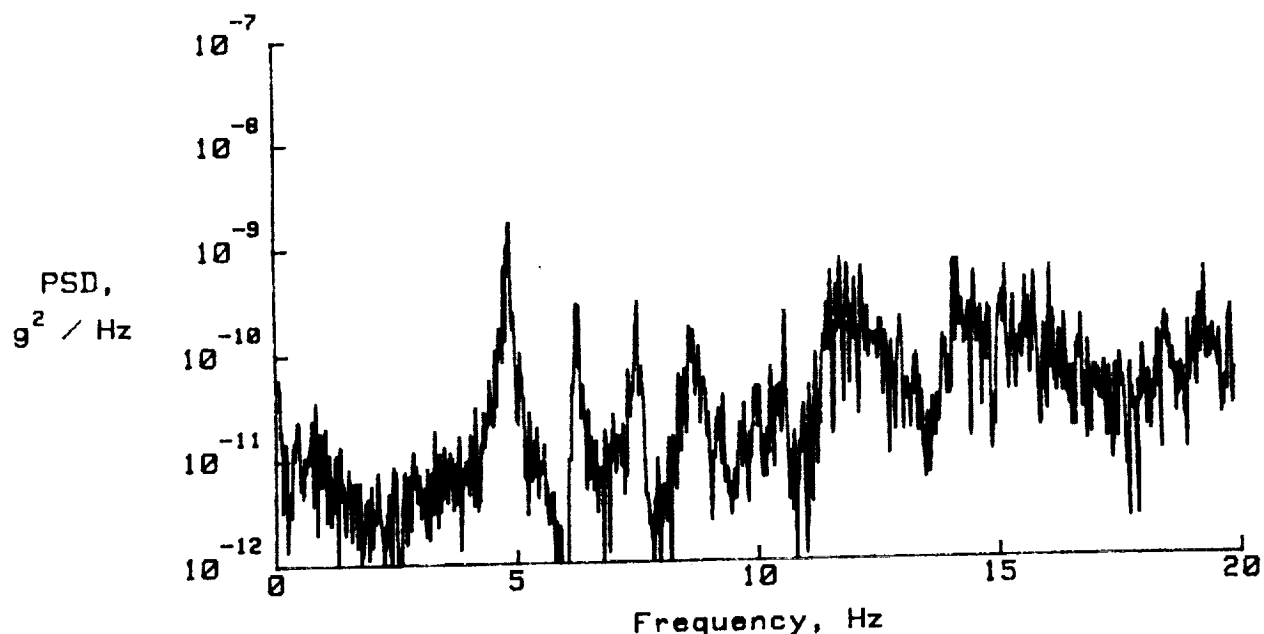
(b) Maneuver segment

Figure 32. Concluded.



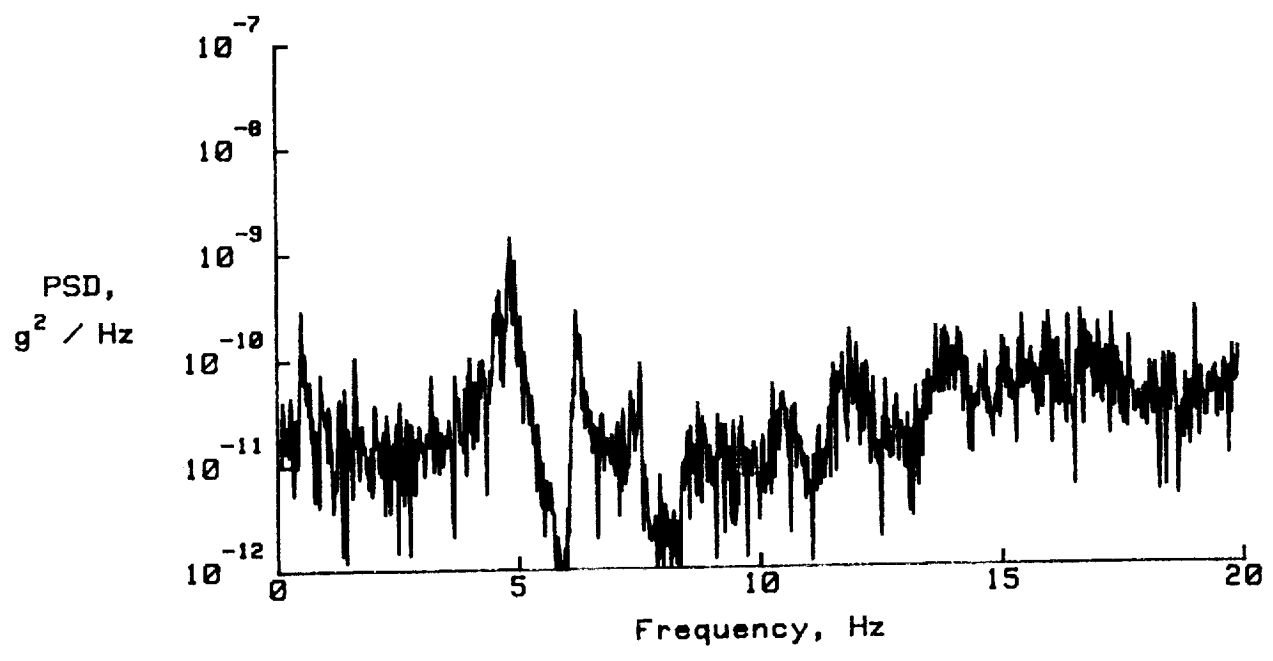
(a) Pre-manuever segment

Figure 33. Unfiltered power spectral density, maneuver 2, Z-axis.



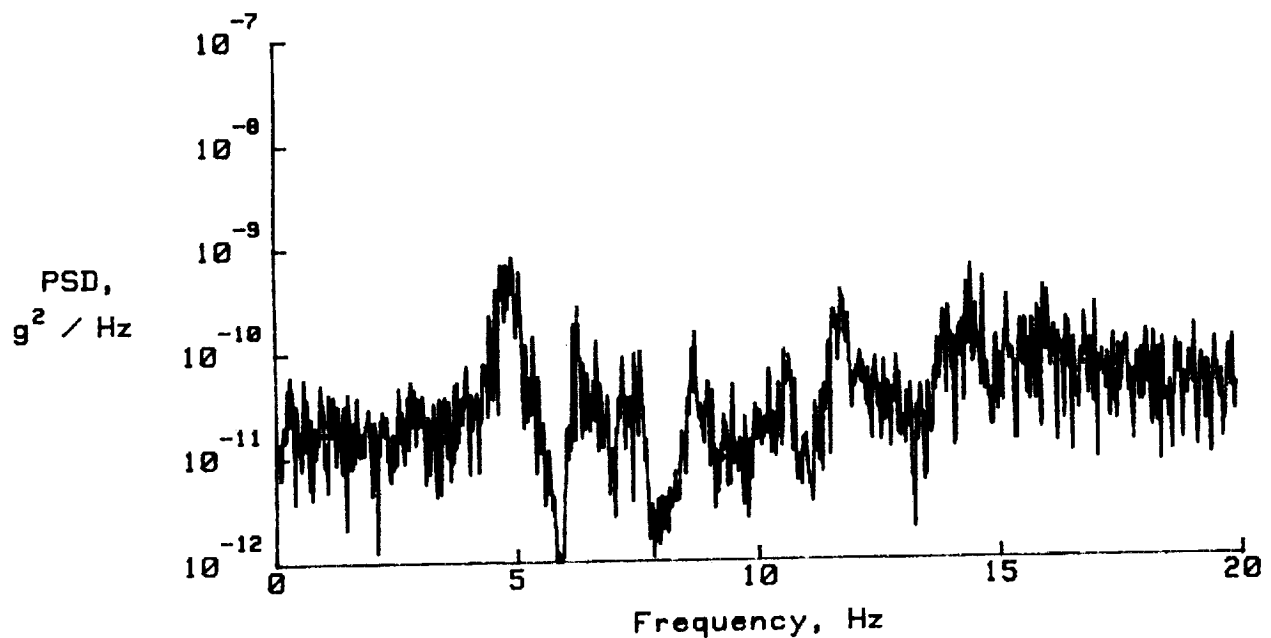
(b) Maneuver segment

Figure 33. Concluded.



(a) Pre-maneuver segment

Figure 34. Unfiltered power spectral density, maneuver 3, Z-axis.



(b) Maneuver segment

Figure 34. Concluded.



Report Documentation Page

1. Report No. NASA TM-102627	2. Government Accession No.	3. Recipient's Catalog No.	
4. Title and Subtitle Determination of Shuttle Orbiter Center of Gravity from Flight Measurements		5. Report Date January 1991	
7. Author(s) E. W. Hinson, J. Y. Nicholson, and R. C. Blanchard		6. Performing Organization Code	
9. Performing Organization Name and Address NASA Langley Research Center Hampton, VA 23665-5225		8. Performing Organization Report No.	
12. Sponsoring Agency Name and Address National Aeronautics and Space Administration Washington, DC 20546-0001		10. Work Unit No. 506-40-91-01	
15. Supplementary Notes E. W. Hinson: ST Systems Corporation, Hampton, Virginia. J. Y. Nicholson: Vigyan Research Associates, Inc., Hampton, Virginia. R. C. Blanchard: Langley Research Center, Hampton, Virginia.		11. Contract or Grant No.	
16. Abstract Flight measurements of pitch, yaw, and roll rates and the resultant rotationally induced linear accelerations during three orbital maneuvers on Shuttle mission STS 61-C have been used to calculate the actual orbiter center-of-gravity location. The calculation technique reduces error due to lack of absolute calibration of the accelerometer measurements and compensates for accelerometer temperature bias and for the effects of gravity gradient. Accuracy of the technique was found to be limited by the nonrandom and asymmetrical distribution of orbiter structural vibration at the accelerometer mounting location. Fourier analysis of the vibration was performed to obtain the power spectral density profiles which show magnitudes in excess of 10^4 $\mu g^2/Hz$ for the actual vibration and over 500 $\mu g^2/Hz$ for the filtered accelerometer measurements. The data from this analysis provide a characterization of the Shuttle acceleration environment which may be useful in future studies related to accelerometer system application and "zero-g" investigations or processes.		13. Type of Report and Period Covered Technical Memorandum	
17. Key Words (Suggested by Author(s)) Accelerometer Center-of-gravity Rotational dynamics		18. Distribution Statement Unclassified-Unlimited Subject Category 34	
19. Security Classif. (of this report) Unclassified	20. Security Classif. (of this page) Unclassified	21. No. of pages 54	22. Price A04